Symmetry transformation and dimensionality reduction of the anisotropic pressure Hessian

M. Carbone[1,2], M. Iovieno[1] and A. D. Bragg[2],†

[1]Dipartimento di Ingegneria Meccanica e Aerospaziale, Politecnico di Torino, Corso Duca degli Abruzzi 24, 10129 Torino, Italy

[2]Department of Civil and Environmental Engineering, Duke University, Durham, NC 27708, USA

The dynamics of the velocity gradient tensor in turbulence is governed in part by the anisotropic pressure Hessian, which is a non-local functional of the velocity gradient field. This anisotropic pressure Hessian plays a key dynamical role, for example in preventing finite-time singularities, but it is difficult to understand and model due to its non-locality and complexity. In this work a symmetry transformation for the pressure Hessian is introduced, such that when the transformation is applied to the original pressure Hessian, the dynamics of the invariants of the velocity gradients remains unchanged. We then exploit this symmetry transformation to perform a dimensional reduction on the three-dimensional anisotropic pressure Hessian, which, remarkably, is possible everywhere in the flow except on zero-measure sets. The dynamical activity of the newly introduced dimensionally reduced anisotropic pressure Hessian is confined to two-dimensional manifolds in the three-dimensional flow, and exhibits striking alignment properties with respect to the strain-rate eigenframe and the vorticity vector. The dimensionality reduction, together with the strong preferential alignment properties, leads to new dynamical insights for understanding and modelling the role of the anisotropic pressure Hessian in three-dimensional turbulent flows.

Key words: turbulence theory, intermittency

---

1. Introduction

The small-scale dynamics of turbulent flows is governed by highly nonlinear and non-local dynamical processes, whose statistics are strongly intermittent in space and time (Yeung, Donzis & Sreenivasan 2012; Buaria *et al.* 2019). Moreover, the strong and intermittent small-scale dynamics can generate coherent structures at larger scales (Majda & Bertozzi 2001; Ibbeken, Green & Wilczek 2019). Such small-scale dynamics is effectively characterized by the velocity gradient field, rather than the velocity field itself (Tsinober 2001). Consequently, understanding and modelling the velocity gradient dynamics is of singular importance in the study of turbulence, and has been the subject of many works in the literature. In particular, the Lagrangian description of the velocity gradient dynamics has proven to be especially fruitful for understanding and modelling

† Email address for correspondence: andrew.bragg@duke.edu

the statistical geometry of turbulence, the rate of deformation of fluid material volumes and intermittency (Meneveau 2011).

The equation governing the velocity gradient tensor dynamics along a fluid particle trajectory is easily derived from the Navier–Stokes equation (NSE) but, the equation is unclosed because of the anisotropic/non-local pressure Hessian and viscous terms. Developing closure models for these complex terms requires insight, and this work concentrates on the properties of the anisotropic pressure Hessian.

The pressure field can be expressed as a linear, non-local, functional of the second invariant of the velocity gradient tensor. Therefore, a strategy to infer the statistical properties of the pressure field consists in analysing how the velocity gradient organizes in space. A quantitative investigation of the correlation length of the velocity gradient magnitude shows that, in rotation-dominated regions, the pressure field is governed by a dissipation-scale neighbourhood while, in strain-dominated regions, the pressure is determined by an inertial-scale neighbourhood (Vlaykov & Wilczek 2019). However, many works in the literature have shown that the pressure statistics can be described reasonably well by quasi-local approximations (Chevillard *et al.* 2008; Lawson & Dawson 2015). Indeed, the long-range contributions to the pressure field are much smaller than expected due to partial cancellation of the competing contributions of the strain rate and vorticity magnitude to the second invariant of the velocity gradient (Vlaykov & Wilczek 2019).

Information about the statistics of the pressure field can be employed to develop closure models for the Lagrangian dynamics of the velocity gradient in turbulence. In the inviscid case, an early closure model by Vieillefosse (1982) was constructed by neglecting the non-local/anisotropic part of the pressure Hessian, while retaining its local/isotropic part. This model is usually referred to as the restricted Euler (RE) model. The RE model led to important insights, showing the tendency for the intermediate eigenvalue of the strain rate to be positive, and also the preferred alignment of the vorticity with the intermediate strain-rate eigenvector (Cantwell 1992) as observed in direct numerical simulation (DNS) of isotropic turbulence and homogeneous shear flows (Ashurst *et al.* 1987). However, the RE flow exhibits a finite-time singularity for almost all initial conditions, indicating that a realistic model for the velocity gradient should take into account the anisotropic pressure Hessian, in addition to viscous contributions. Indeed, the anisotropic pressure Hessian is considered to play a major role in preventing such finite-time singularities, even for ideal fluids, and it has been analysed in detail in several works (Ohkitani 1993; Nomura & Post 1998; Chevillard *et al.* 2008; Vlaykov & Wilczek 2019).

In an early work, the anisotropic pressure Hessian was modelled as a stochastic process, independent of the gradient dynamics, and the stochastic differential equations for the velocity gradient were constructed to satisfy isotropy and empirical constraints, such as log-normality of the dissipation rate (Girimaji & Pope 1990). A more advanced phenomenological and stochastic model was constructed in Chertkov, Pumir & Shraiman (1999) by analysing the Lagrangian dynamics using four tracer trajectories, forming a tetrad. The tetrad can be used to construct a scale-dependent filtered velocity gradient (Naso & Pumir 2005) and the closure of the model involves a direct relation between the local pressure and the velocity gradient on the tetrad. The tetrad model provided a phenomenological basis for understanding how the anisotropic pressure Hessian acts to reduce nonlinearity in the flow, a property that also emerges in more systematic closures for the pressure Hessian based on Gaussian random fields (Wilczek & Meneveau 2014).

The deformation history of a fluid particle in the flow has been employed to model the anisotropic pressure Hessian and viscous terms using Lagrangian coordinate closures (Chevillard & Meneveau 2006). In this model, only information on the recent fluid

deformation is retained, that is, the dynamics is affected by times up to the Kolmogorov time scale, τ_η, in the past. A phenomenological closure is then constructed assuming that at a time τ_η in the past, the Lagrangian pressure Hessian was isotropic. This model does not exhibit the singularity associated with the RE, and was shown to capture many of the non-trivial features of the velocity gradient dynamics that are observed in experiments and DNSs of the NSE. However, it displays unphysical behaviour for flows at large Reynolds number. A critical comparison with DNS data (Chevillard *et al.* 2008) showed that while the closure model presented in Chevillard & Meneveau (2006) can reproduce some of the non-trivial velocity gradient dynamics, it misses some important features of the pressure Hessian dynamics and statistical geometry in the flow.

Wilczek & Meneveau (2014) proposed a closure for the Lagrangian velocity gradient equation by assuming that the velocity is a random field with Gaussian statistics. Closed expressions for the pressure Hessian and viscous terms conditioned on the velocity gradient are obtained by means of the characteristic functional of the Gaussian velocity field. The model produces qualitatively good results but, owing to the Gaussian assumption, it leads to quantitative predictions that are not in full agreement with DNS data. Therefore, to correct this aspect, the authors modified the closure such that the mathematical structure was retained, but the coefficients appearing in the model were prescribed using DNS data. This led to significant improvements, and the model provides interesting insights into the role of the anisotropic pressure Hessian in preventing the singularities arising in the RE. However, the enhanced model did not satisfy the kinematic relations for incompressible and isotropic flows (Betchov 1956).

Another model has been developed by Johnson & Meneveau (2016), who combined the closure modelling ideas by both Chevillard & Meneveau (2006) and Wilczek & Meneveau (2014). This model leads to improvements compared with the two models on which it is based, and it is formulated in such a way that by construction the model satisfies the kinematic relations of Betchov (1956). However, a quantitative comparison with DNS data revealed some shortcomings in the ability of the model to properly capture the intermittency of the flow. Moreover, it runs into difficulties for high Reynolds number flows, like that of Chevillard & Meneveau (2006) from which it has been partly derived. The capability to reproduce intermittency and high Reynolds number flow features is a major challenge for velocity gradient models. A recent development of velocity gradient models, based on a multiscale refined self-similarity hypothesis, proposed by Johnson & Meneveau (2017), seems to remove the Reynolds number limitations.

In summary, while significant progress has been made since the initial modelling efforts of Vieillefosse (1982, 1984), much remains to be done. A major difficulty in developing accurate closure approximations for the Lagrangian velocity gradient equation is that the dynamical effects of the anisotropic/non-local pressure Hessian on the flow are not yet fully understood and are difficult to approximate using simple closure ideas. This fact is the motivation behind the present work which aims to improve the understanding of the anisotropic pressure Hessian, and in particular, its statistical geometry relative to the strain-rate and vorticity fields. In the following, we present what appears to be a previously unrecognized symmetry transformation for the pressure Hessian, such that when this transformation is applied to the pressure Hessian, the invariant dynamics of the velocity gradient tensor remains unchanged. We then exploit this symmetry transformation to perform a dimensional reduction on the anisotropic pressure Hessian. Remarkably, this dimensional reduction can be performed everywhere in the turbulent flow, except on zero-measure sets, and produces the newly introduced dimensionally reduced anisotropic pressure Hessian which lives on a two-dimensional manifold and exhibits striking alignment properties with respect to the strain-rate eigenframe and

the vorticity vector. This dimensionality reduction, together with evident preferential alignments of the dimensionally reduced anisotropic pressure Hessian has significant implications for understanding and modelling the anisotropic pressure Hessian in turbulent flows.

2. Theory

In this section the symmetry transformation for the dynamics of the velocity gradient invariants is derived from the velocity gradient equations written in the eigenframe of the strain-rate tensor. The symmetry transformation is then exploited to reduce the rank of the anisotropic pressure Hessian, leading to a dimensionally reduced anisotropic pressure Hessian, that is, to a two-dimensional object embedded in a three-dimensional space.

2.1. *Equations for the velocity gradient in the strain-rate eigenframe*

The three-dimensional flow of a Newtonian and incompressible fluid is described by the Navier–Stokes equations

$$\nabla \cdot \boldsymbol{u} = 0, \tag{2.1a}$$

$$D_t \boldsymbol{u} \equiv \partial_t \boldsymbol{u} + (\boldsymbol{u} \cdot \nabla) \boldsymbol{u} = -\nabla P + \nu \nabla^2 \boldsymbol{u}, \tag{2.1b}$$

where $\boldsymbol{u}(\boldsymbol{x}, t)$ is the velocity field, $P(\boldsymbol{x}, t) = p(\boldsymbol{x}, t)/\rho$ is the ratio between the pressure p and the density ρ and ν is the kinematic viscosity. By taking the gradient of (2.1), the equations for the velocity gradient tensor $\boldsymbol{A} \equiv \nabla \boldsymbol{u}$ are obtained:

$$\text{Tr}(\boldsymbol{A}) = 0, \tag{2.2a}$$

$$D_t \boldsymbol{A} = -\boldsymbol{A} \cdot \boldsymbol{A} - \boldsymbol{H} + \nu \nabla^2 \boldsymbol{A}, \tag{2.2b}$$

where $\text{Tr}(\cdot)$ indicates the matrix trace and $\boldsymbol{H} \equiv \nabla \nabla P$ is the pressure Hessian. With respect to the standard basis of the three-dimensional space $\{\boldsymbol{e}_i\}$, the velocity gradient and pressure Hessian are $\boldsymbol{A} = \partial_j u_i \boldsymbol{e}_i \boldsymbol{e}_j^\top$ and $\boldsymbol{H} = \partial_j \partial_i P \boldsymbol{e}_i \boldsymbol{e}_j^\top$, where $\cdot^\top$ indicates transposition and repeated indexes are contracted. Here and throughout, '$\cdot$' denotes the standard inner/matrix–matrix product, e.g. $\boldsymbol{A} \cdot \boldsymbol{A} = A_{ij} A_{jk} \boldsymbol{e}_i \boldsymbol{e}_k^\top$, while '$:$' denotes a double inner product, e.g. $\boldsymbol{A} : \boldsymbol{A} = \text{Tr}(\boldsymbol{A} \cdot \boldsymbol{A}) = A_{ij} A_{ji}$.

The velocity gradient is decomposed into its symmetric part, the strain-rate tensor $\boldsymbol{S} \equiv (\boldsymbol{A} + \boldsymbol{A}^\top)/2 = (A_{ij} + A_{ji}) \boldsymbol{e}_i \boldsymbol{e}_j^\top/2$, and anti-symmetric part, the rotation-rate tensor $\boldsymbol{R} \equiv (\boldsymbol{A} - \boldsymbol{A}^\top)/2 = (A_{ij} - A_{ji}) \boldsymbol{e}_i \boldsymbol{e}_j^\top/2$, which is associated with the vorticity, $\boldsymbol{\omega} \equiv \nabla \cdot \boldsymbol{u}$. The vorticity components in the standard basis are $\omega_i = \epsilon_{ikj} R_{jk}$, where ϵ_{ijk} is the permutation symbol. The equations for the strain rate and vorticity are derived from the symmetric and anti-symmetric parts of (2.2):

$$\text{Tr}(\boldsymbol{S}) = 0, \tag{2.3a}$$

$$D_t \boldsymbol{S} = -\boldsymbol{S} \cdot \boldsymbol{S} + \boldsymbol{R} \cdot \boldsymbol{R}^\top - \boldsymbol{H} + \nu \nabla^2 \boldsymbol{S}, \tag{2.3b}$$

$$D_t \boldsymbol{\omega} = \boldsymbol{S} \cdot \boldsymbol{\omega} + \nu \nabla^2 \boldsymbol{\omega}. \tag{2.3c}$$

It is insightful to write (2.3) in the strain-rate eigenframe. The strain rate in its eigenframe is $\boldsymbol{S} = \Lambda_{ij} \boldsymbol{v}_i \boldsymbol{v}_j^\top$, where Λ_{ij} is a diagonal matrix containing the strain-rate eigenvalues λ_i on its diagonal, and $\boldsymbol{v}_i$ are the strain-rate eigenvectors. The strain-rate eigenvectors $\boldsymbol{v}_i$

are orthogonal with unit length, and they form an orthonormal and right-oriented basis for the three-dimensional Euclidean space, that is $\boldsymbol{v}_i^\top \cdot \boldsymbol{v}_j = \delta_{ij}$ where δ_{ij} is the Kronecker delta. The basis $\{\boldsymbol{v}_i\}$ is related to the standard basis $\{\boldsymbol{e}_j\}$ by the rotation matrix $\boldsymbol{V}$, whose ith column contains the components of the ith strain-rate eigenvector with respect to the standard basis,

$$V_{ji} \equiv \boldsymbol{e}_j^\top \cdot \boldsymbol{v}_i, \tag{2.4}$$

so that $\boldsymbol{v}_i = V_{ji}\boldsymbol{e}_j$. The strain-rate eigenframe undergoes a rigid body rotation with angular velocity $\boldsymbol{w}$. The eigenvectors $\{\boldsymbol{v}_i\}$ remain orthonormal and right-oriented for all times and therefore the angular velocity $\boldsymbol{w}$ is the same for all the eigenvectors, which evolve according to a pure rotation defined by $D_t\boldsymbol{v}_i \equiv \boldsymbol{w} \times \boldsymbol{v}_i$. The components of $\boldsymbol{w}$ in the strain-rate eigenframe are $\tilde{w}_i = \epsilon_{ijk}\boldsymbol{v}_j^\top \cdot D_t\boldsymbol{v}_k/2$, where here and throughout, the tilde on a variable denotes its components in the strain-rate eigenframe. The components of the strain-rate angular velocity, $\tilde{w}_i$, are associated with the components of the anti-symmetric tensor $\widetilde{W}_{ij} = \epsilon_{ikj}\tilde{w}_k$, with $\widetilde{W}_{ij}$ defined in terms of the strain-rate eigenvectors as

$$\widetilde{W}_{ij} \equiv \boldsymbol{v}_i^\top \cdot D_t\boldsymbol{v}_j, \tag{2.5}$$

so that $D_t\boldsymbol{v}_i = \widetilde{W}_{ji}\boldsymbol{v}_j$. The full anti-symmetric tensor whose components are defined by (2.5) is denoted by $\boldsymbol{W} = \widetilde{W}_{ij}\boldsymbol{v}_i\boldsymbol{v}_j^\top$.

The time derivative of the strain rate $\boldsymbol{S} = \Lambda_{ij}\boldsymbol{v}_i\boldsymbol{v}_j^\top$ can be expressed in the strain-rate eigenframe using (2.5)

$$D_t\boldsymbol{S} = \left(D_t\Lambda_{ij}\right)\boldsymbol{v}_i\boldsymbol{v}_j^\top + \left(\widetilde{W}_{ik}\Lambda_{kj} - \Lambda_{ik}\widetilde{W}_{kj}\right)\boldsymbol{v}_i\boldsymbol{v}_j^\top. \tag{2.6}$$

The variation of the strain-rate tensor is due to two contributions. The first term on the right-hand side of (2.6) is diagonal and is generated by the variation of the strain-rate eigenvalues. The second term on the right-hand side of (2.6) is generated by the rotation of the strain-rate eigenframe. The part in parentheses is equal to the eigenframe components of the commutator of $\boldsymbol{W}$ and $\boldsymbol{S}$:

$$[\boldsymbol{W}, \boldsymbol{S}] = \boldsymbol{W} \cdot \boldsymbol{S} - \boldsymbol{S} \cdot \boldsymbol{W}. \tag{2.7}$$

The components of the commutator $[\boldsymbol{W}, \boldsymbol{S}]$ in the strain-rate eigenframe can be rewritten as

$$\boldsymbol{v}_i^\top \cdot [\boldsymbol{W}, \boldsymbol{S}] \cdot \boldsymbol{v}_j = \widetilde{W}_{ik}\Lambda_{kj} - \Lambda_{ik}\widetilde{W}_{kj} = \left(\lambda_{(j)} - \lambda_{(i)}\right)\widetilde{W}_{ij}, \tag{2.8}$$

where indexes enclosed by parentheses are not contracted. This result shows that the commutator $[\boldsymbol{W}, \boldsymbol{S}]$ has no diagonal components in the eigenframe, so that (2.6) may be decomposed into a diagonal part due only to the variation of the strain-rate eigenvalues, and a off-diagonal part due only to the rotation of the strain-rate eigenvectors.

Just as for the strain-rate equation, (2.5) can also be used to write the vorticity equation in the strain-rate eigenframe

$$D_t\boldsymbol{\omega} = (D_t\widetilde{\omega}_i)\,\boldsymbol{v}_i + \left(\widetilde{W}_{ij}\widetilde{\omega}_j\right)\boldsymbol{v}_i, \tag{2.9}$$

where $\widetilde{\omega}_i = \boldsymbol{v}_i^\top \cdot \boldsymbol{\omega}$ are the vorticity components in the strain-rate eigenframe. In (2.9), $\widetilde{W}_{ij}\widetilde{\omega}_j$ corresponds to the vortex tilting term and quantifies the rate of change of the components of vorticity in the strain-rate eigenframe because of the rotation of the strain-rate eigenframe with time.

Using (2.6) and (2.9) we may express the velocity gradient dynamics (2.3) in the strain-rate eigenframe

$$\sum_{i=1}^{3} \lambda_i = 0, \tag{2.10a}$$

$$D_t \lambda_i = -\lambda_i^2 + \frac{1}{4}\left(\omega^2 - \widetilde{\omega}_i^2\right) - \widetilde{H}_{i(i)} + \nu \widetilde{\nabla^2 S}_{i(i)}, \tag{2.10b}$$

$$(\lambda_{(j)} - \lambda_{(i)})\widetilde{W}_{ij} = -\frac{1}{4}\widetilde{\omega}_i\widetilde{\omega}_j - \widetilde{H}_{ij} + \nu\widetilde{\nabla^2 S}_{ij}, \quad \text{for } i > j, \tag{2.10c}$$

$$D_t\widetilde{\omega}_i = \lambda_{(i)}\widetilde{\omega}_i - \widetilde{W}_{ij}\widetilde{\omega}_j + \nu\widetilde{\nabla^2\omega}_i, \tag{2.10d}$$

where λ_i are the strain-rate eigenvalues, $\omega^2 \equiv \widetilde{\omega}_i\widetilde{\omega}_i$ is the enstrophy and indexes in parentheses are not contracted. The tilde indicates tensor components in the strain-rate eigenframe, so that

$$\widetilde{H}_{ij} = \boldsymbol{v}_i^\top \cdot \boldsymbol{H} \cdot \boldsymbol{v}_j, \quad \widetilde{\nabla^2 S}_{ij} = \boldsymbol{v}_i^\top \cdot \left(\nabla^2 \boldsymbol{S}\right) \cdot \boldsymbol{v}_j, \quad \widetilde{\nabla^2\omega}_i = \boldsymbol{v}_i^\top \cdot \left(\nabla^2\boldsymbol{\omega}\right). \tag{2.11a–c}$$

Equation (2.10a) is simply the eigenframe form of the continuity equation (2.3a). Equation (2.10b) describes the evolution of the strain-rate eigenvalues, and emerges from the diagonal part of (2.3b) in the strain-rate eigenframe: the terms on the right-hand side of (2.10b) describe the rate of variation of the eigenvalues due to strain self-amplification, the centrifugal force due to the rotation of the fluid element about its vorticity axis, and the contributions of the diagonal components of the pressure Hessian and viscous stress, respectively. Equation (2.10c) describes the rotation of the strain-rate eigenvectors, and emerges from the off-diagonal part of (2.3b) in the strain-rate eigenframe. The terms on the right-hand side of (2.10c) describe the rotation of the strain-rate eigenframe due to the misalignment between the vorticity and the strain-rate eigenvectors (in the sense that, if $\boldsymbol{\omega}$ were perfectly aligned with $\boldsymbol{v}_i$, then $\widetilde{\omega}_i\widetilde{\omega}_j = 0$ for $i > j$), the off-diagonal terms of the pressure Hessian and of the viscous stress, respectively. The eigenvalue difference $\lambda_{(j)} - \lambda_{(i)}$ that appears on the left-hand side of (2.10c) represents the resistance of the strain-rate eigenframe to rotation (Vieillefosse 1982), acting as a moment of inertia.

Equation (2.10d) describes the evolution of the vorticity components in the strain-rate eigenframe, and is obtained from (2.3c). The terms on the right-hand side of (2.10d) describe the rate of variation of the vorticity components due to vortex stretching, vortex tilting caused by the rotation of the strain-rate eigenframe, and due to the anti-symmetric part of the viscous stress. It should be noted that, as shown in Nomura & Post (1998), the viscous contribution from (2.10c) to the vortex tilting term $\widetilde{W}_{ij}\widetilde{\omega}_j$ cancels out with part of the contribution coming from $\nu\widetilde{\nabla^2\omega}_i$. Due to this cancellation, the viscous forces do not ultimately contribute explicitly to the vortex tilting process, and in view of this, Nomura & Post (1998) re-express (2.10d) in terms of an effective rotation-rate of the eigenframe that is independent of viscosity. We choose to retain the equations in the form stated above, which makes clear that the rotation rate of the eigenframe does depend on the viscous stress in the fluid, even if viscous effects do not ultimately contribute to the process of vortex tilting.

The eigenframe equations (2.10) provide an insightful tool to analyse the velocity gradients in turbulence, allowing to disentangle various processes, and their properties have been studied in detail by Vieillefosse (1982), Dresselhaus & Tabor (1992) and Nomura & Post (1998).

2.2. *A new symmetry for the dynamics of the velocity gradient invariants*

The eigenframe equations satisfy a number of symmetries. They are naturally invariant under the transformation $\widetilde{\omega}_i \to -\widetilde{\omega}_i$, since the eigenvectors are only defined up to an arbitrary sign. The inviscid equations are also formally invariant under time reversal $t \to -t$. In addition, the equations possess another kind of symmetry that does not appear to have been previously recognized. This new symmetry arises from the fact that in the equation governing $\widetilde{\omega}_i$, namely (2.10d), the angular velocity of the strain-rate eigenframe $\boldsymbol{w}$ only enters through the cross-product $\boldsymbol{w} \times \boldsymbol{\omega} = \widetilde{W}_{ij}\widetilde{\omega}_j \boldsymbol{v}_i$, and therefore the component of $\boldsymbol{w}$ along the vorticity direction, $\boldsymbol{w} \cdot \boldsymbol{\omega}$, does not affect the dynamical evolution of the eigenframe variables.

In order to introduce the new symmetry we first define the transformation

$$\boldsymbol{W} \to \boldsymbol{W} + \gamma \boldsymbol{R}, \tag{2.12}$$

where $\gamma(\boldsymbol{x}, t)$ is a non-dimensional, real scalar field. Transformation (2.12) corresponds to $\boldsymbol{w} \to \boldsymbol{w} + \gamma \boldsymbol{\omega}/2$, and therefore adds to the angular velocity of the strain-rate eigenframe an additional rotation rate about the vorticity axis with magnitude $\gamma \|\boldsymbol{\omega}\|/2$. Equation (2.12) implies a transformation of the time derivative of the velocity gradient tensor, which we analyse in detail in the following.

When transformation (2.12) is introduced into the strain-rate time derivative (2.6), the strain-rate time derivative transforms as

$$\mathrm{D}_t\boldsymbol{S} \to \mathrm{D}_t\boldsymbol{S} + \gamma\left(\widetilde{R}_{ik}\Lambda_{kj} - \Lambda_{ik}\widetilde{R}_{kj}\right)\boldsymbol{v}_i\boldsymbol{v}_j^\top, \tag{2.13}$$

or, equivalently,

$$\mathrm{D}_t\boldsymbol{S} \to \mathrm{D}_t\boldsymbol{S} + \gamma[\boldsymbol{R}, \boldsymbol{S}], \tag{2.14}$$

where $[\boldsymbol{R}, \boldsymbol{S}] = \boldsymbol{R} \cdot \boldsymbol{S} - \boldsymbol{S} \cdot \boldsymbol{R}$ is the commutator between the anti-symmetric and symmetric parts of the velocity gradient. Since the diagonal components of the commutator $[\boldsymbol{R}, \boldsymbol{S}]$ are zero in the strain-rate eigenframe, then the equations for the strain-rate eigenvalues ((2.10a) and (2.10b)) are not affected by the additional term in (2.13). Therefore, when the transformation (2.12) is introduced into the eigenframe equations (2.10), the equations governing the strain-rate eigenvalues ((2.10a) and (2.10b)) remain unchanged. However, the transformation (2.12) does affect the off-diagonal part of the strain-rate equation since the off-diagonal components of $[\boldsymbol{R}, \boldsymbol{S}]$ are in general non-zero in the strain-rate eigenframe. As a result, under the transformation (2.12), (2.10c) becomes

$$\left(\lambda_{(j)} - \lambda_{(i)}\right)\widetilde{W}_{ij} = -\frac{1}{4}\widetilde{\omega}_i\widetilde{\omega}_j - \widetilde{H}_{ij} - \gamma\widetilde{R}_{ij}\left(\lambda_{(j)} - \lambda_{(i)}\right) + \widetilde{\nu\nabla^2 S}_{ij}, \quad i > j. \tag{2.15}$$

The transformation from (2.10c) to (2.15) results in a time-dependent modification of the orientation of the strain-rate eigenframe with respect to a fixed reference frame. However, this change of orientation of the strain-rate eigenvectors, introduced by (2.12), is not relevant for the dynamics of the velocity gradient invariants, that are independent of the orientation of the strain-rate eigenframe with respect to a fixed basis.
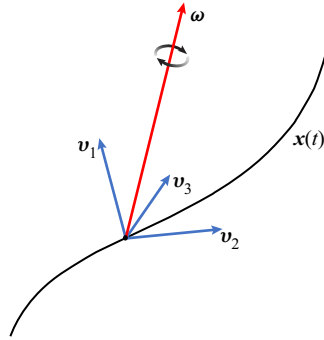
FIGURE 1. Schematic to illustrate the symmetry transformation. At any point along a fluid particle trajectory $x(t)$ (or equivalently, at any fixed point in space), the rotation rate of the strain-rate eigenframe (formed by the blue lines) may be modified by adding an arbitrary rotation about the vorticity axis (red line), without affecting the dynamical evolution of either the eigenvalues λ_i or the vorticity components in the eigenframe $\widetilde{\omega}_i$.

When the transformation (2.12) is introduced into the vorticity time derivative (2.9), then the vorticity time derivative transforms as

$$\mathrm{D}_t\boldsymbol{\omega} \to \mathrm{D}_t\boldsymbol{\omega} + \gamma \left(\widetilde{R}_{ij}\widetilde{\omega}_j\right) \boldsymbol{v}_i = \mathrm{D}_t\boldsymbol{\omega}, \tag{2.16}$$

since, by definition, $\boldsymbol{R} \cdot \boldsymbol{\omega} = \boldsymbol{0}$. Therefore, (2.10$d$) remains unchanged

$$\mathrm{D}_t\widetilde{\omega}_i = \lambda_{(i)}\widetilde{\omega}_i - \left(\widetilde{W}_{ij} + \gamma\widetilde{R}_{ij}\right)\widetilde{\omega}_j + \nu\widetilde{\nabla^2\omega_i} = \lambda_{(i)}\widetilde{\omega}_i - \widetilde{W}_{ij}\widetilde{\omega}_j + \nu\widetilde{\nabla^2\omega_i}. \tag{2.17}$$

In view of this, transformation (2.12) does not affect the dynamics of either λ_i or $\widetilde{\omega}_i$, that is, the transformation $\boldsymbol{W} \to \boldsymbol{W} + \gamma\boldsymbol{R}$ is a symmetry transformation for λ_i and $\widetilde{\omega}_i$. This symmetry arises because the rotation rate of the eigenframe about the vorticity axis is a redundant degree of freedom as far as the dynamical evolution of λ_i and $\widetilde{\omega}_i$ is concerned. In figure 1 we provide a schematic to illustrate the symmetry transformation.

Before proceeding further, it is worth mentioning how the dynamical symmetry just introduced also relates to the dynamics of other invariants of the velocity gradient $\boldsymbol{A}$. As discussed in Meneveau (2011), for an incompressible flow, $\boldsymbol{A}$ may be described in terms of the three strain-rate eigenvectors $\boldsymbol{v}_1, \boldsymbol{v}_2, \boldsymbol{v}_3$ and five invariant quantities (Cantwell 1992)

$$\mathcal{Q} \equiv -A_{ij}A_{ji}/2, \quad \mathcal{R} \equiv -A_{ij}A_{jk}A_{ki}/3,$$
$$\mathcal{Q}_S \equiv -S_{ij}S_{ij}/2, \quad \mathcal{R}_S \equiv -S_{ij}S_{jk}S_{ki}/3, \quad \mathcal{V}^2 \equiv \omega_i S_{ij}S_{jk}\omega_k. \tag{2.18a--e}$$

These five invariants can be written in terms of λ_i and $\widetilde{\omega}_i$ (which are five independent quantities due to incompressibility), e.g.

$$\mathcal{Q} = -\sum_i \lambda_i^2/2 + \sum_i \widetilde{\omega}_i^2/4, \quad \mathcal{R} = -\sum_i \lambda_i^3/3 - \sum_i \lambda_i\widetilde{\omega}_i^2/4. \tag{2.19a,b}$$

Therefore the symmetry transformation for λ_i and $\widetilde{\omega}_i$ also implies the same symmetry transformation for $\mathcal{Q}, \mathcal{R}, \mathcal{Q}_S, \mathcal{R}_S, \mathcal{V}^2$. That is, the dynamical evolution of the set of invariants $\mathcal{Q}, \mathcal{R}, \mathcal{Q}_S, \mathcal{R}_S, \mathcal{V}^2$ is unaffected by the transformation $\boldsymbol{W} \to \boldsymbol{W} + \gamma\boldsymbol{R}$.

It is important to note that, while the dynamical evolution of the single-time/single-point invariants $\mathcal{Q}, \mathcal{R}, \mathcal{Q}_S, \mathcal{R}_S, \mathcal{V}^2$ is not affected by the symmetry transformation (2.12),

multi-time/multi-point invariants are in general affected. For example, the invariant $\text{Tr}(\boldsymbol{S}(\boldsymbol{x}, t) \cdot \boldsymbol{S}(\boldsymbol{x}', t'))$ is affected by the transformation (2.12) since in general the transformation arbitrarily modifies the relative orientations of the eigenframes of $\boldsymbol{S}(\boldsymbol{x}, t)$ and $\boldsymbol{S}(\boldsymbol{x}', t')$. Nevertheless, the dynamical evolution of multi-time or multi-point products of $\lambda_i, \widetilde{\omega}_i$ is not affected by the symmetry transformation. Multi-time statistics are relevant in a number of fundamental research areas, for example in the framework of Lagrangian refined similarity hypothesis (Yu & Meneveau 2010) or Lagrangian chaos (Johnson & Meneveau 2015), and also in applied research areas, as for sub-Kolmogorov droplet deformation (Biferale, Meneveau & Verzicco 2014) and rod/disk spinning and tumbling (Chevillard & Meneveau 2013). In those contexts, it is important for models to reproduce multi-time statistics. The new symmetry presented in this work may preserve some multi-time statistics for appropriate choices of the multiplier γ since that additional degree of freedom may be fixed in the most convenient way, based on the field of application. In which way, and to what extent, the presented symmetry carries over to situations in which multi-time statistics are important deserves further investigation, but it is left for future work. In this paper we focus on single-point and single-time quantities.

2.3. *Symmetry transformation for the anisotropic pressure Hessian*

The anisotropic/non-local pressure Hessian is defined as

$$\mathcal{H} \equiv \boldsymbol{H} - \text{Tr}(\boldsymbol{H})\frac{\boldsymbol{I}}{3}, \tag{2.20}$$

which satisfies $\text{Tr}(\mathcal{H}) = 0$, and contains all of the non-local part of $\boldsymbol{H}$. The property that the dynamical evolution of λ_i and $\widetilde{\omega}_i$ is not affected by the transformation (2.12) can be interpreted as a symmetry transformation for $\mathcal{H}$. To see this, we note that, under the transformation $\boldsymbol{W} \rightarrow \boldsymbol{W} + \gamma \boldsymbol{R}$, the equation for $\boldsymbol{A}$ becomes

$$\text{D}_t \boldsymbol{A} = -\boldsymbol{A} \cdot \boldsymbol{A} - \boldsymbol{H} - \gamma[\boldsymbol{R}, \boldsymbol{S}] + \nu \nabla^2 \boldsymbol{A}. \tag{2.21}$$

We may then group together $\gamma[\boldsymbol{R}, \boldsymbol{S}]$ and $\mathcal{H}$ to define a transformed anisotropic pressure Hessian

$$\mathcal{H}_\gamma \equiv \mathcal{H} + \gamma[\boldsymbol{R}, \boldsymbol{S}]. \tag{2.22}$$

The crucial point is that introducing the transformation $\mathcal{H} \rightarrow \mathcal{H}_\gamma$ corresponds to introducing the transformation $\boldsymbol{W} \rightarrow \boldsymbol{W} + \gamma \boldsymbol{R}$ into the velocity gradient dynamics, which leaves the dynamical evolution of λ_i and $\widetilde{\omega}_i$ unchanged. The additional term $[\boldsymbol{R}, \boldsymbol{S}]$ in (2.22) is symmetric and traceless, such that $\mathcal{H}_\gamma$ preserves the properties of the original anisotropic pressure Hessian $\mathcal{H}$. Moreover, the symmetry transformation (2.22) holds for all real and finite values of $\gamma(\boldsymbol{x}, t)$, which at this stage is still undetermined.

It is interesting to note that the commutator between the anti-symmetric and symmetric parts of the velocity gradient $[\boldsymbol{R}, \boldsymbol{S}]$ also arises in the expression for the pressure Hessian obtained in closure models assuming a random velocity field with Gaussian statistics (Wilczek & Meneveau 2014). In the framework of the Gaussian closure, the coefficient of $[\boldsymbol{R}, \boldsymbol{S}]$ is the only one that requires specific knowledge of the spatial structure of the flow and must be prescribed by phenomenological closure hypothesis, while all other coefficients of the model can be determined exactly. However, our analysis implies that the ability of the Gaussian closure to predict the dynamics of λ_i and $\widetilde{\omega}_i$ will not be impacted by the phenomenological closure hypothesis.

2.4. *Using the symmetry transformation for dimensionality reduction*

While any finite and real γ in (2.22) provides a suitable $\mathcal{H}_\gamma$, there may exist certain choices of γ that generate configurations of the transformed pressure Hessian $\mathcal{H}_\gamma$ that reside on a lower-dimensional manifold in the system, in the sense that some of its eigenvalues are zero. If such configurations exist and are common, this could significantly aid understanding and modelling the complexity of the anisotropic pressure Hessian. To seek for lower-dimensional configurations is equivalent to seeking for configurations in which a rank-reduction on $\mathcal{H}_\gamma$ can be performed. We denote the dimensionally reduced form of $\mathcal{H}_\gamma$ by $\mathcal{H}_\gamma^*$. Notice that $\mathcal{H}_\gamma^*$ cannot have rank one since $\mathrm{Tr}(\mathcal{H}_\gamma) = 0$, and therefore either $\mathrm{rk}(\mathcal{H}_\gamma^*) = 2$ or $\mathcal{H}_\gamma^* = \mathbf{0}$.

In seeking for lower-dimensional configurations of the anisotropic pressure Hessian, when $\mathcal{H}$ is singular (i.e. its rank is less than three and it has at least one zero eigenvalue) the additional term involving $[\mathbf{R}, \mathbf{S}]$ in (2.22) is not needed, since $\mathcal{H}$ already lives on a lower-dimensional space and we take $\mathcal{H}_\gamma^* = \mathcal{H}$, which corresponds to $\gamma = 0$. On the other hand, when $\mathcal{H}$ is not singular we seek for a non-zero vector z_2 such that $\mathcal{H}_\gamma^* \cdot z_2 = \mathbf{0}$, where z_2 corresponds to the eigenvector of $\mathcal{H}_\gamma^*$ associated with its zero (and intermediate) eigenvalue. This is equivalent to the generalized eigenvalue problem $\det(\mathcal{H}_\gamma^*) = 0$, that is,

$$\det\left(\mathbf{I} + \gamma \mathcal{H}^{-1} \cdot [\mathbf{R}, \mathbf{S}]\right) = 0. \tag{2.23}$$

Notice that $\mathcal{H}$ can be safely inverted in (2.23), since the case of singular $\mathcal{H}$ has been already taken into account and corresponds to $\gamma = 0$. If there exist finite and real values for γ that solve (2.23), then those values of γ generate a rank-two $\mathcal{H}_\gamma^*$. Defining $\mathcal{E} \equiv \mathcal{H}^{-1} \cdot [\mathbf{R}, \mathbf{S}]$, the characteristic equation for γ is

$$a\gamma^3 + b\gamma^2 + c\gamma + 1 = 0, \tag{2.24}$$

with real coefficients a, b, c given by

$$a \equiv \det(\mathcal{E}), \quad b \equiv \frac{1}{2}\left(\mathrm{Tr}(\mathcal{E})^2 - \mathrm{Tr}(\mathcal{E} \cdot \mathcal{E})\right), \quad c \equiv \mathrm{Tr}(\mathcal{E}). \tag{2.25a–c}$$

The properties of the roots of (2.24) are determined by the discriminant of the polynomial

$$\Delta \equiv b^2 c^2 - 4ac^3 - 4b^3 - 27a^2 - 18abc. \tag{2.26}$$

When $\Delta = 0$, all of the roots of (2.24) are real and at least two are equal, when $\Delta > 0$ there are three distinct real roots, and when $\Delta < 0$ there is one real root and two complex conjugate roots. In every case, provided that $a \neq 0$, there is at least one real root since all the coefficients are real and the degree of the characteristic polynomial is odd. When $a = 0$, a real and finite root γ may or may not exist according to the value of the discriminant Δ. This shows that configurations where a rank-two $\mathcal{H}_\gamma$ does not exist, that is, the pressure Hessian is intrinsically three-dimensional, may only occur when $a = 0$. Interestingly, $a \equiv \det \mathcal{H}^{-1} \det[\mathbf{R}, \mathbf{S}]$ (by hypothesis $\det \mathcal{H} \neq 0$) and the dimensional reduction of the anisotropic pressure Hessian may not be performed where $\det[\mathbf{R}, \mathbf{S}] = 0$. The determinant of this commutator can be expressed in terms of the eigenframe variables as

$$\det[\mathbf{R}, \mathbf{S}] = \frac{1}{4}(\lambda_2 - \lambda_1)(\lambda_3 - \lambda_2)(\lambda_1 - \lambda_3)\widetilde{\omega}_1\widetilde{\omega}_2\widetilde{\omega}_3, \tag{2.27}$$

so that, when either one or more of the vorticity components in the strain-rate eigenframe is zero, and/or the strain-rate configuration is axisymmetric, a singular $\mathcal{H}_\gamma$ may not exist. However, since λ_i and $\widetilde{\omega}_i$ have continuous probability distributions, then the probability that $\det[\boldsymbol{R}, \boldsymbol{S}] = 0$ is in fact zero. Therefore, the dimensional reduction of $\mathcal{H}_\gamma$ is possible everywhere in the flow except on sets of zero measure.

When (2.24) admits more than one real and finite solution then multiple dimensionally reduced anisotropic pressure Hessians can be defined at the same point, that is, there exist more than a single real and finite multiplier γ such that $\mathcal{H}_\gamma$ has rank less than three. In this configuration, different $\mathcal{H}_\gamma^*$ can generate the same dynamics of the velocity gradient invariants. We fix this additional degree of freedom by choosing the value of γ that provides the maximum alignment between the intermediate eigenvector of the dimensionally reduced anisotropic pressure Hessian and the vorticity. As it will be shown in §3, this is justified on the basis of the numerical results, which indicate a marked preferential alignment of the intermediate eigenvector of the dimensionally reduced anisotropic pressure Hessian with the vorticity.

The dimensional reduction of the anisotropic pressure Hessian, defined through (2.23), allows for a noticeable reduction of the complexity of the anisotropic pressure Hessian leading to a better understanding of its dynamical effects. Indeed, the fully three-dimensional anisotropic pressure Hessian is specified by five real numbers, being a square matrix of size three. In particular, it takes two numbers to specify the normalized eigenvector $\boldsymbol{y}_1$, one additional number for $\boldsymbol{y}_2$ (then $\boldsymbol{y}_3$ is automatically determined) and two more numbers for the independent eigenvalues φ_1 and φ_3 (since $\sum_i \varphi_i = 0$). Therefore, the anisotropic pressure Hessian can be expressed in its eigenframe as

$$\mathcal{H} = \sum_{i=1}^{3} \varphi_i \boldsymbol{y}_i \boldsymbol{y}_i^\top. \tag{2.28}$$

We keep the standard convention $\varphi_1 \geq \varphi_2 \geq \varphi_3$. On the other hand, the dimensionally reduced anisotropic pressure Hessian is specified by only four real numbers. Indeed it is a traceless and singular square matrix of size three. In particular, it takes two numbers to specify the plane orthogonal to the normalized eigenvector $\boldsymbol{z}_2$ an additional number to specify the orientation of $\boldsymbol{z}_1$ on the plane orthogonal to $\boldsymbol{z}_2$ (then $\boldsymbol{z}_3$ is determined) and a number for the single independent eigenvalue ψ. Therefore, the dimensionally reduced anisotropic pressure Hessian can be expressed in its eigenframe as

$$\mathcal{H}_\gamma^* = \psi \left(\boldsymbol{z}_1 \boldsymbol{z}_1^\top - \boldsymbol{z}_3 \boldsymbol{z}_3^\top \right), \tag{2.29}$$

since the intermediate eigenvector is identically zero and the others satisfy $\psi_1 = -\psi_3 = \psi$ with $\psi \geq 0$. The pressure Hessian $\mathcal{H}_\gamma^*$ resides locally on the plane Π_2 orthogonal to $\boldsymbol{z}_2$, which is the tangent space to a more complex manifold. Indeed, the tensor $\mathcal{H}_\gamma^*$ acts on a generic vector $\boldsymbol{q}$ amplifying its component along $\boldsymbol{z}_1$, cancelling its component along $\boldsymbol{z}_2$ and amplifying and flipping its component along $\boldsymbol{z}_3$. The dimensionally reduced anisotropic pressure Hessian is effective only on the plane Π_2. The eigenvalue of the dimensionally reduced anisotropic pressure Hessian can be related to the full anisotropic pressure Hessian and the vorticity since $\omega_i \mathcal{H}_{ij} \omega_j = \omega_i \mathcal{H}_{\gamma,ij}^* \omega_j$, which implies

$$\psi = \frac{\sum_i \varphi_i (\boldsymbol{y}_i^\top \cdot \boldsymbol{\omega})^2}{(\boldsymbol{z}_1^\top \cdot \boldsymbol{\omega})^2 - (\boldsymbol{z}_3^\top \cdot \boldsymbol{\omega})^2}. \tag{2.30}$$
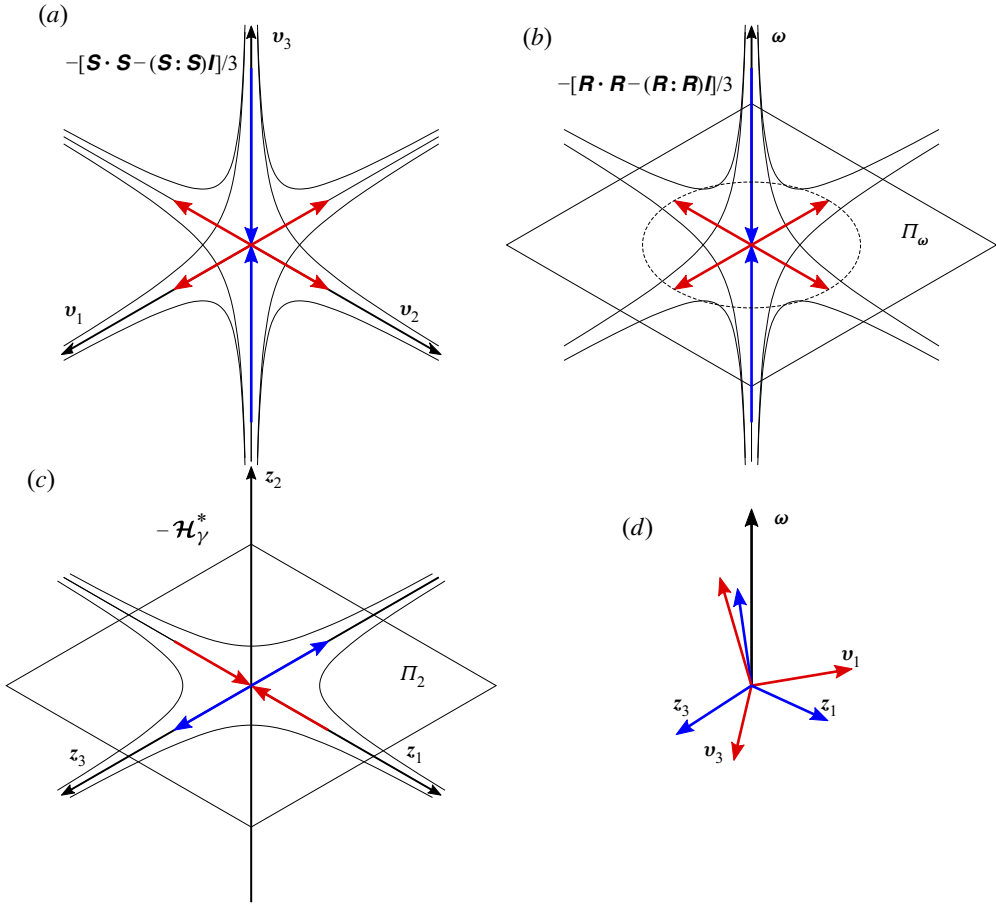
FIGURE 2. Schematic representation of contribution of the terms on the right-hand side of (2.32). (*a*) Strain-rate term $-[\boldsymbol{S}\cdot\boldsymbol{S}-\mathrm{Tr}(\boldsymbol{S}\cdot\boldsymbol{S})\boldsymbol{I}/3]$ for the typical configuration $\lambda_1=\lambda_2=-\lambda_3/2$. (*b*) Rotation term $-[\boldsymbol{R}\cdot\boldsymbol{R}-\mathrm{Tr}(\boldsymbol{R}\cdot\boldsymbol{R})\boldsymbol{I}/3]$ which isotropically produces stretching rate along the plane orthogonal to $\boldsymbol{\omega}$ and a compression parallel to $\boldsymbol{\omega}$. (*c*) Dimensionally reduced anisotropic pressure Hessian $-\mathcal{H}_\gamma^*$ which stretches the fluid element along the z_3 direction and compresses it along the z_1 direction. (*d*) Typical configuration for the relative orientation of strain-rate eigenframe, vorticity and dimensionally reduced anisotropic pressure Hessian eigenframe.

Moreover, the tensors $\mathcal{H}$ and $\mathcal{H}_\gamma^*$ satisfy the relation $\omega_i S_{ij}\mathcal{H}_{jk}\omega_k=\omega_i S_{ij}\mathcal{H}_{\gamma,jk}^*\omega_k$ which yields another equation for the eigenvalue ψ:

$$\psi=\frac{\sum_i\varphi_i(\boldsymbol{\omega}^\top\cdot\boldsymbol{S}\cdot\boldsymbol{y}_i)(\boldsymbol{y}_i^\top\cdot\boldsymbol{\omega})}{(\boldsymbol{\omega}^\top\cdot\boldsymbol{S}\cdot\boldsymbol{z}_1)(\boldsymbol{z}_1^\top\cdot\boldsymbol{\omega})-(\boldsymbol{\omega}^\top\cdot\boldsymbol{S}\cdot\boldsymbol{z}_3)(\boldsymbol{z}_3^\top\cdot\boldsymbol{\omega})}. \tag{2.31}$$

Equation (2.30) shows that a perfect alignment between z_2 and $\boldsymbol{\omega}$ would result in an infinitely large ψ, unless the anisotropic pressure Hessian fulfils the condition $\boldsymbol{\omega}^\top\cdot\mathcal{H}\cdot\boldsymbol{\omega}=0$. For example, such a peculiar configuration occurs when the flow is exactly two-dimensional, for which $\mathcal{H}_\gamma^*=\mathcal{H}$. In general, a large eigenvalue ψ corresponds to strong alignment between z_2 and $\boldsymbol{\omega}$, as will be discussed in §3.

This dimensionality reduction brings two-dimensional features into three-dimensional flows, and it is interesting to note that the equations for the velocity gradient already contain another two-dimensional flow feature. In particular, the term $(\omega^2 - \widetilde{\omega}_i^2)/4$ in (2.10b) arises from the eigenframe representation of $\boldsymbol{R} \cdot \boldsymbol{R} = -\omega^2 \boldsymbol{P_\omega}/4$, where $\boldsymbol{P_\omega}$ is the projection tensor on the plane $\Pi_{\boldsymbol{\omega}}$ orthogonal to the vorticity vector $\boldsymbol{\omega}$. This term describes the straining motion in the plane orthogonal to $\boldsymbol{\omega}$ that is associated with the centrifugal force produced by the spinning of the fluid particle about its vorticity axis. As we will discuss later, this two-dimensional effect can be compared with the two-dimensional effect of $\mathcal{H}_\gamma^*$ on the velocity gradient evolution, leading to interesting insights into their respective dynamical roles. Moreover, $\mathcal{H}_\gamma^*$ is a two-dimensional object in a three-dimensional space which opens the possibility to effectively compare pressure Hessian statistics between two-dimensional and three-dimensional flows. However, the tangent space to the manifold defined by $\mathcal{H}_\gamma^*$ varies in space and time, therefore the flow on Π_2 cannot be directly compared with Euclidean two-dimensional turbulence but with flows in more complex geometries (Falkovich & Gawędzki 2014).

Using the dynamical equivalence of $\mathcal{H}$ and $\mathcal{H}_\gamma^*$, we may re-write the equation governing λ_i (2.10b) as (ignoring the viscous term)

$$\mathrm{D}_t \lambda_i = -\left(\lambda_i^2 - \frac{1}{3} \sum_j \lambda_j^2 \right) - \frac{1}{4} \left(\widetilde{\omega}_i^2 - \frac{1}{3} \sum_j \widetilde{\omega}_j^2 \right) - \widetilde{\mathcal{H}}_{\gamma, i(i)}^*, \qquad (2.32)$$

and in figure 2 we provide a schematic to illustrate the role of each of the terms on the right-hand side of (2.32).

3. Numerical results: dimensionally reduced anisotropic pressure Hessian

We now turn to assess the properties of $\mathcal{H}_\gamma^*$, using data from a DNS of statistically stationary, isotropic turbulence. The DNS data used are those by Ireland, Bragg & Collins (2016a,b), at a Taylor microscale Reynolds number $R_\lambda = 597$. The data have been obtained through a pseudo-spectral method to solve the incompressible NSE on a three-dimensional, triperiodic cube discretized with 2048^3 grid points. A deterministic forcing method that preserves the kinetic energy in the flow has been employed. A detailed description of the numerical method used can be found in Ireland *et al.* (2013).

In addition to the DNS results, we also present some of the results obtained by using a surrogate Gaussian field, which has been generated by randomizing the phases of the DNS velocity field while retaining the Fourier amplitudes from the DNS. Constructed in this way, the actual and surrogate velocity fields have the same dissipation rate, characteristic time scale τ_η and energy spectrum as the DNS field. The comparison between this Gaussian surrogate field and the DNS dataset can provide insights into the extent to which the observed behaviour is kinematic (i.e. found even in the surrogate field) or truly dynamical in origin. Where appropriate, some of the surrogate field results are discussed in the main paper, while others are shown in the Appendix.

3.1. *Pressure Hessian dimensional reduction*

We first consider the properties of real and finite multipliers γ, as determined by the numerical solution of (2.24). At each grid point we solve the generalized eigenvalue problem (2.23) to determine real and finite multipliers γ for which $\mathcal{H}_\gamma^*$ is singular. In particular, the LAPACK dggev subroutine (Anderson *et al.* 1999) has been used to
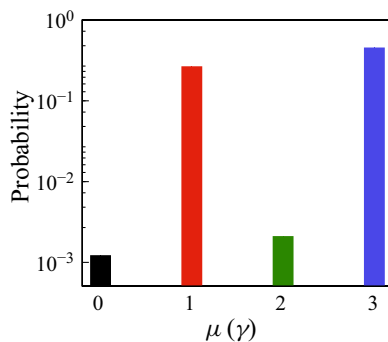
FIGURE 3. Probability of multiplicity of real and finite roots of (2.24).

solve the characteristic equation (2.24). The roots of the characteristic equation are in general complex numbers $\widetilde{\gamma} = (\alpha_R + \sqrt{-1}\alpha_I)/\beta$, where α_R, α_I and β are real numbers. The numerical solution of (2.24) is ill-conditioned when $\det \mathcal{H}^{-1} \det[\boldsymbol{R}, \boldsymbol{S}]$ is very small and the division by β should be performed carefully. Therefore, at each grid point we first check that $|\beta| > T_1$ (threshold $T_1 = 10^{-6}$ has been used for the present results) and then we check that $|\alpha_I/\alpha_R| < T_2$ (threshold $T_2 = 10^{-10}$ has been employed). The tolerance thresholds T_i are absolute numbers since γ is non-dimensional. We confirmed that the results are only weakly sensitive to these small tolerance values and we monitored that $\det \mathcal{H}_\gamma^*$ is actually zero up to the numerical roundoff error.

Figure 3 shows the probability of the multiplicity of real and finite values of γ obtained by solving (2.24). All the statistics have been computed by averaging the flow over space and time, a total of ten snapshots spanning six eddy turnover times have been used. The dimensionally reduced anisotropic pressure Hessian exists at the vast majority of the grid points, the configurations with no real and finite multipliers is observed at only about 0.1 % of the grid points and corresponds to very small values of $\det \mathcal{H}^{-1} \det[\boldsymbol{R}, \boldsymbol{S}]$ in the numerical simulation. The most common case ($\sim$60 % of the data) corresponds to three real multipliers γ, that is, three dynamically equivalent pressure Hessians which generate the same dynamics of the velocity gradient invariants. The next most common case ($\sim$40 % of the data) is a single real root γ and a single rank-two $\mathcal{H}_\gamma^*$. The case with two real and finite roots (and the third root asymptotically small compared with these) is rare ($\sim$0.15 % of the data) and corresponds to $\det[\boldsymbol{R}, \boldsymbol{S}]$ close to zero. In the configurations in which there exist multiple values of γ, the multiplier which gives the highest alignment between the vorticity vector and the intermediate eigenvector of the dimensionally reduced anisotropic pressure Hessian is selected. Indeed, that preferential alignment is a clear feature of the dimensionally reduced anisotropic pressure Hessian, as we will see below.

In figure 4 we show a two-dimensional snapshot of the multiplier field $\gamma(\boldsymbol{x}, t)$ for which $\mathcal{H}_\gamma$ has rank two, for both the DNS and the surrogate field. As expected, the field $\gamma(\boldsymbol{x}, t)$ exhibits a much greater spatial structure in the DNS as compared with the surrogate field, showing how the dimensionality reduction of the anisotropic pressure Hessian depends upon the local structure of the flow. Indeed, since $\gamma(\boldsymbol{x}, t)$ is obtained through the solution of (2.24), the spatial variation of $\gamma(\boldsymbol{x}, t)$ will reflect the spatial variation of the coefficients of its polynomial equation, and these coefficients depend upon the velocity gradient field.

The probability density function (PDF) of the multiplier γ for which $\mathcal{H}_\gamma$ has rank two is shown in figure 5(*a*). The PDF of γ is highly non-Gaussian and γ can be very large, even if with a small probability. This may be due to the intermittency of the velocity gradient field, however, since γ is obtained from a polynomial equation that
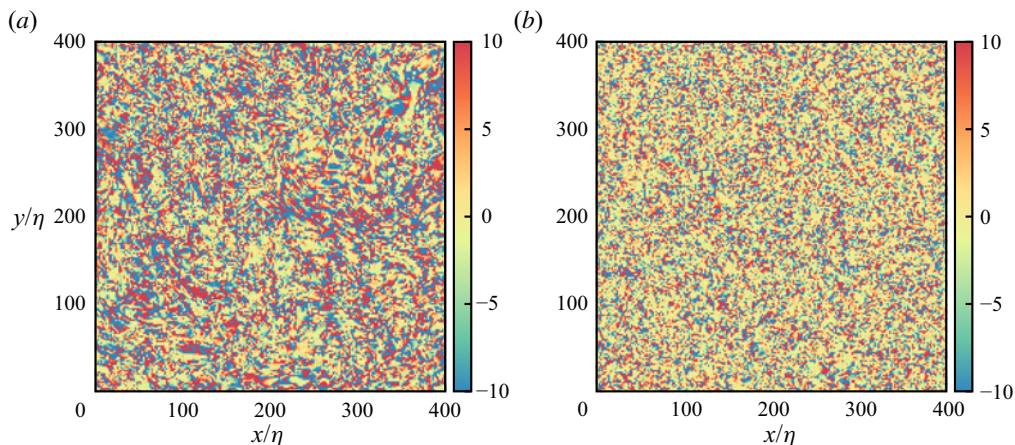
FIGURE 4. Two-dimensional snapshot of the multiplier field $\gamma(\boldsymbol{x}, t)$ for (*a*) the actual DNS field and (*b*) for the surrogate Gaussian field. Colours correspond to the values of $\gamma(\boldsymbol{x}, t)$.

depends nonlinearly on the velocity gradients, this nonlinear dependence may also be a cause of the observed non-Gaussianity. As shown in the Appendix, the PDF of γ is also non-Gaussian even for the surrogate field; however, the non-Gaussianity is much weaker than in the DNS. Therefore, a substantial source of the non-Gaussianity observed for the PDF of γ in the DNS does indeed arise for the dynamical intermittency in the velocity gradients. Another possible source of the strong non-Gaussianity of γ would be the high probability of small values of $\det[\boldsymbol{R}, \boldsymbol{S}]$. In such a case, the matrix used for the reduction, $[\boldsymbol{R}, \boldsymbol{S}]$, would span the whole three-dimensional domain but with a very small eigenvalue in a certain eigendirection. As a consequence, in order to perform the dimensionality reduction on $\mathcal{H}_\gamma \equiv \mathcal{H} + \gamma[\boldsymbol{R}, \boldsymbol{S}]$, the multiplier γ must be large enough so that $\gamma[\boldsymbol{R}, \boldsymbol{S}]$ can compensate the component of $\mathcal{H}$ in that eigendirection, and that component may be large. The PDF of $\det[\boldsymbol{R}, \boldsymbol{S}]$ is shown in figure 5(*b*). The results show that $\det[\boldsymbol{R}, \boldsymbol{S}]$ is highly intermittent, being small throughout the vast majority of the flow, but exhibiting extreme fluctuations in very small regions. Indeed, $\det[\boldsymbol{R}, \boldsymbol{S}]$ is a sixth-order moment of the velocity gradient field. Moreover, the tendency for small values of $\det[\boldsymbol{R}, \boldsymbol{S}]$ can also be understood in terms of the well-known fact that $\boldsymbol{\omega}$ tends to misalign with $\boldsymbol{v}_3$ (Meneveau 2011), leading to small values for $\widetilde{\omega}_3$ and therefore to small values of $\det[\boldsymbol{R}, \boldsymbol{S}]$ via (2.27). Both of these explanations are supported by the fact that, as shown in the Appendix, the PDF for $\det[\boldsymbol{R}, \boldsymbol{S}]$ obtained from the surrogate field is almost Gaussian, and there is no preferential alignment of $\boldsymbol{\omega}$ with $\boldsymbol{v}_3$ in the surrogate field.

We now turn to investigate flow features conditioned on $\det[\boldsymbol{R}, \boldsymbol{S}]$. The high probability of observing small values of $\det[\boldsymbol{R}, \boldsymbol{S}]$ is consistent with the average of the strain rate and rotation magnitude conditioned on the local value of $\det[\boldsymbol{R}, \boldsymbol{S}]$, the results for which are shown in figure 5(*c*). The values of $\tau_\eta^2 \|\boldsymbol{S}\|^2$ and $\tau_\eta^2 \|\boldsymbol{R}\|^2$ when $\det[\boldsymbol{R}, \boldsymbol{S}] \to 0$, where τ_η is the Kolmogorov time scale, are both slightly less than $1/2$, where $1/2$ is the precise value of the unconditioned averages $\tau_\eta^2 \langle \|\boldsymbol{S}\|^2 \rangle = \tau_\eta^2 \langle \|\boldsymbol{R}\|^2 \rangle$ in isotropic turbulence. For larger values of $\det[\boldsymbol{R}, \boldsymbol{S}]$, $\|\boldsymbol{R}\|^2$ has a well-defined power law scaling, $\|\boldsymbol{R}\|^2 \sim |\det[\boldsymbol{R}, \boldsymbol{S}]|^{1/3}$, as shown in the inset of figure 5(*c*). The power law exponent $1/3$ is consistent with simple dimensional analysis. On the other hand, while $\|\boldsymbol{S}\|^2$ also depends on $\det[\boldsymbol{R}, \boldsymbol{S}]$ as a power law, the exponent is less than $1/3$, and cannot be predicted by simple dimensional analysis. This is somewhat reminiscent of the results in Buaria *et al.* (2019) for $\langle \|\boldsymbol{R}\|^2 | \|\boldsymbol{S}\|^2 \rangle$ and
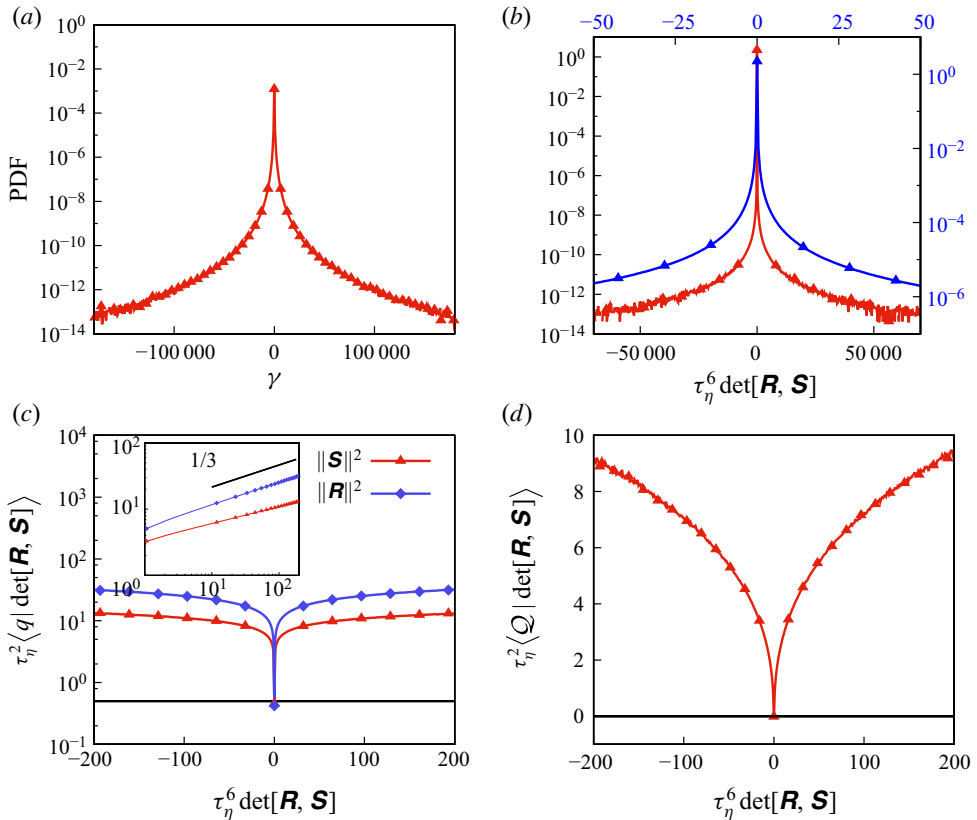
FIGURE 5. (*a*) Probability density function of the real multiplier γ. (*b*) The PDF of the determinant of the commutator of anti-symmetric and symmetric part of the velocity gradient, $\det[\boldsymbol{R}, \boldsymbol{S}]$, the blue curve refers to the blue labels and represents the same PDF over a smaller range. (*c*) Strain-rate magnitude $\|\boldsymbol{S}\|^2$ and rotation magnitude $\|\boldsymbol{R}\|^2$ conditioned on $\det[\boldsymbol{R}, \boldsymbol{S}]$, the same plot in logarithmic scale is in the inset. (*d*) Second invariant of the velocity gradient tensor $\mathcal{Q}$ conditioned on $\det[\boldsymbol{R}, \boldsymbol{S}]$.

$\langle \|\boldsymbol{S}\|^2 | \|\boldsymbol{R}\|^2 \rangle$, where they found that the former was well described by dimensional analysis (i.e. by Kolmogorov's 1941 theory, see Pope 2000), while the latter was not. The average of the second invariant of the velocity gradient tensor $\mathcal{Q}$ conditioned on the local value of $\det[\boldsymbol{R}, \boldsymbol{S}]$ is shown in figure 5(*d*). Interestingly, the region where $\det[\boldsymbol{R}, \boldsymbol{S}]$ is small is slightly strain-rate dominated (i.e. $\mathcal{Q} < 0$). On the other hand, in the regions where $|\det[\boldsymbol{R}, \boldsymbol{S}]|$ is relatively large, the dynamics is clearly rotation-dominated (i.e. $\mathcal{Q} > 0$). When the conditioned average of $\mathcal{Q}$ is weighted with the PDF of $\det[\boldsymbol{R}, \boldsymbol{S}]$ and integrated over all $\det[\boldsymbol{R}, \boldsymbol{S}]$ it yields $\langle \mathcal{Q} \rangle = 0$ for isotropic turbulence, which indicates the very large relative weight of regions of the flow contributing to $\langle \mathcal{Q} | \det[\boldsymbol{R}, \boldsymbol{S}] \rangle$ being negative and very small.

3.2. *Dimensionally reduced anisotropic pressure Hessian eigenvalue*

Figures 6(*a*) and 6(*b*) show that, whereas $\mathcal{H}$ is in general a fully three-dimensional object with three non-zero eigenvalues φ_i that satisfy $\sum_{i=1}^3 \varphi_i = 0$, $\mathcal{H}_\gamma^*$ is a two-dimensional object with only two active eigenvalues that satisfy $\psi_1 = -\psi_3 = \psi$, the intermediate
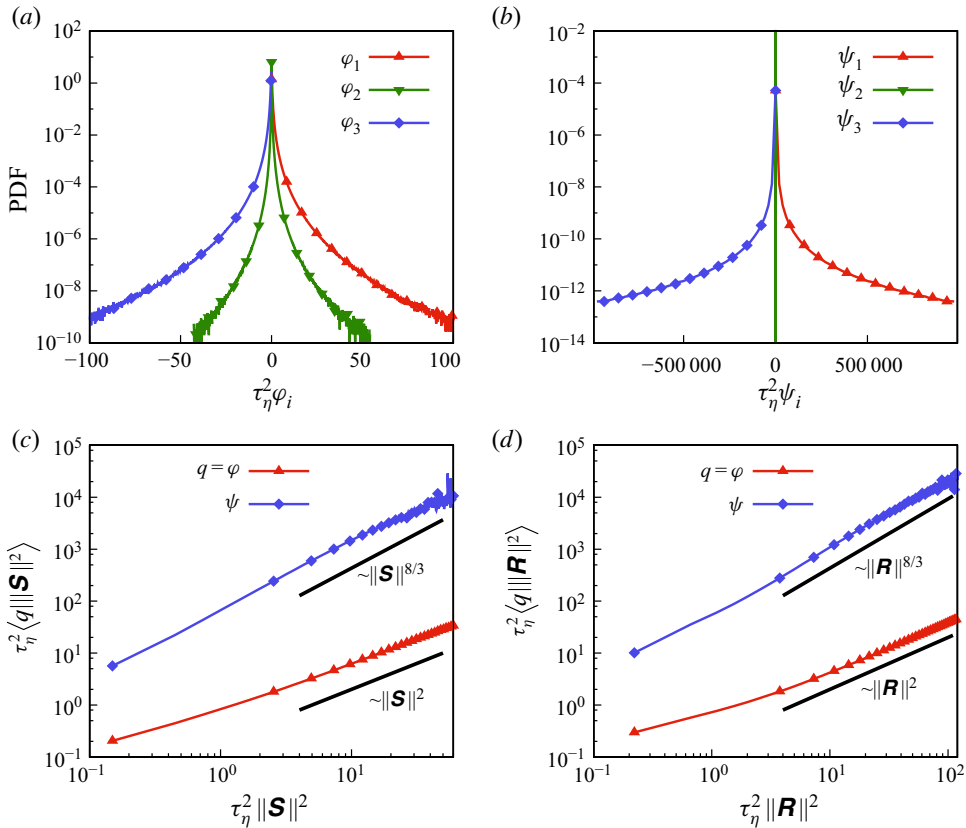
FIGURE 6. Probability density function of the eigenvalues of (*a*) $\mathcal{H}$ and (*b*) eigenvalues of $\mathcal{H}_\gamma^*$, normalized with the Kolmogorov time scale τ_η. (*c*) Magnitude of the anisotropic pressure Hessian eigenvalues $\varphi = \sqrt{\sum_i \varphi_i^2}$ and anisotropic pressure Hessian eigenvalue, ψ, conditioned on the local strain-rate magnitude and (*d*) on the rotation-rate magnitude.

eigenvalue being by construction identically zero, $\psi_2 = 0$. Note that here and throughout, all eigenvectors are unitary, and are ordered so that $\varphi_1 \geq \varphi_2 \geq \varphi_3$. The PDFs of the eigenvalues $\varphi_1 \geq 0$ and $\varphi_3 \leq 0$ of the anisotropic pressure Hessian display marked tails and are almost symmetric with respect to each other. On the contrary, the PDF of φ_2 has moderate tails and it is positively skewed. The eigenvalue of the dimensionally reduced anisotropic pressure Hessian, ψ, exhibits very large fluctuations. Its PDF has wide tails which show that ψ, even if with small probability, can take extremely large values. This is in part due to the large intermittency of the flow, giving rise to large values of $[\boldsymbol{R}, \boldsymbol{S}]$ and γ (although with small probability). The large values observed for ψ are also closely related to the statistical geometry in the system. Indeed, the denominator in (2.30) can be very small because, as it will be shown in the next section, the vorticity tends to strongly align with z_2, inducing large values of ψ. Therefore, the geometrical simplification obtained by replacing the three-dimensional $\mathcal{H}$ with the two-dimensional $\mathcal{H}_\gamma^*$ also comes with the cost that the eigenvalue of $\mathcal{H}_\gamma^*$ is far more intermittent than those of $\mathcal{H}$.

Next, we condition the eigenvalues of $\mathcal{H}$ and $\mathcal{H}_\gamma^*$ on the magnitude of the local strain rate and vorticity $\|\boldsymbol{S}\|^2$ and $\|\boldsymbol{R}\|^2$. For the anisotropic pressure Hessian we define

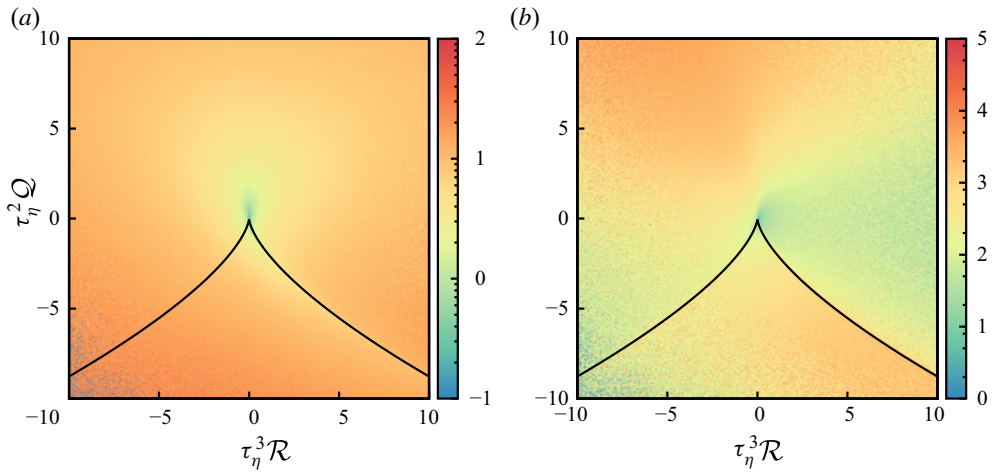FIGURE 7. Results for (*a*) $\langle\varphi|\mathcal{R},\mathcal{Q}\rangle$, where $\varphi = \sqrt{\sum_i \varphi_i^2}$, and (*b*) $\langle\psi|\mathcal{R},\mathcal{Q}\rangle$ as functions of $\mathcal{R}, \mathcal{Q}$. Colours denote the magnitude of the terms, and black lines denote the Vieillefosse tails.

$\varphi = \sqrt{\sum_i \varphi_i^2}$ and compute the conditional averages $\langle\varphi|\|\boldsymbol{S}\|^2\rangle$ and $\langle\varphi|\|\boldsymbol{R}\|^2\rangle$. Similarly, for the dimensionally reduced anisotropic pressure Hessian we look at $\langle\psi|\|\boldsymbol{S}\|^2\rangle$ and $\langle\psi|\|\boldsymbol{R}\|^2\rangle$. The results from the DNS are shown in figures 6(*c*) and 6(*d*). The results reveal a simple scaling $\langle\varphi|\|\boldsymbol{S}\|^2\rangle \sim \|\boldsymbol{S}\|^2$, as dimensional analysis suggests. This lends support to models such as Wilczek & Meneveau (2014), in which the pressure Hessian is a linear combination of $\boldsymbol{S}^2$, $\boldsymbol{R}^2$ and $[\boldsymbol{R}, \boldsymbol{S}]$. The scaling $\langle\varphi|\|\boldsymbol{S}\|^2\rangle \sim \|\boldsymbol{S}\|^2$ is evident especially for large values of $\|\boldsymbol{S}\|^2$. This may reflect the idea that during large fluctuations, the length scale associated with $\boldsymbol{S}$ is smaller as compared to situations where $\boldsymbol{S}$ is small or moderate. If true, then the pressure Hessian is more localized during large fluctuations, giving rise to the scaling $\langle\varphi|\|\boldsymbol{S}\|^2\rangle \sim \|\boldsymbol{S}\|^2$ that reflects a local relationship between φ and $\|\boldsymbol{S}\|^2$. On the other hand, for the dimensionally reduced anisotropic pressure Hessian eigenvalue we find $\langle\psi|\|\boldsymbol{S}\|^2\rangle \sim \|\boldsymbol{S}\|^{2\zeta}$ with $\zeta > 1$ (in particular ζ between 4/3 and 5/4). Nevertheless, $\langle\psi|\|\boldsymbol{S}\|^2\rangle$ maintains a well-defined power law trend, which has positive implications for modelling the anisotropic pressure Hessian using information inferred by the dimensionally reduced anisotropic pressure Hessian. Moreover, the scalings of the conditioned eigenvalue magnitudes are the same whether conditioned on either $\|\boldsymbol{S}\|^2$ or $\|\boldsymbol{R}\|^2$, for both $\mathcal{H}$ and $\mathcal{H}_\gamma^*$.

In figure 7 we plot the conditioned averages $\langle\varphi|\mathcal{R},\mathcal{Q}\rangle$ and $\langle\psi|\mathcal{R},\mathcal{Q}\rangle$. The results show that $\langle\varphi|\mathcal{R},\mathcal{Q}\rangle$ is quite large everywhere except for small $\mathcal{R}, \mathcal{Q}$ and its shape shares similarities with the sheared drop shape of the joint PDF of the invariants $\mathcal{R}, \mathcal{Q}$, that is in figure 12(*d*). In contrast, $\langle\psi|\mathcal{R},\mathcal{Q}\rangle$ is largest in the quadrants $\mathcal{Q} > 0, \mathcal{R} < 0$ and $\mathcal{Q} < 0, \mathcal{R} > 0$ (especially below the right Vieillefosse tail) corresponding to regions of enstrophy and strain-rate production. Therefore, it is not only that the magnitudes of $\mathcal{H}$ and $\mathcal{H}_\gamma^*$ differ significantly, but also that they are most active in different regions of the flow. Indeed, $\mathcal{H}_\gamma^*$ is most active in the regions where the velocity gradients are also most active, while $\mathcal{H}$ is active and strong in many regions where the velocity gradients display relatively little activity (e.g. the quadrant $\mathcal{Q} < 0, \mathcal{R} < 0$). In this sense then, one might say that $\mathcal{H}_\gamma^*$ is more closely tied to the dynamics of the velocity gradients than $\mathcal{H}$.

4. Numerical results: statistical geometry

We now turn to consider the statistical geometry of the system. In figure 8 we show the alignment between the vorticity $\boldsymbol{\omega}$ and the eigenframes of $\mathcal{H}$ and $\mathcal{H}_\gamma^*$. While there is a strong preferential statistical alignment of the intermediate strain-rate eigenvector $\boldsymbol{v}_2$ with $\boldsymbol{\omega}$ (Meneveau 2011), the preferential statistical alignment between $\boldsymbol{\omega}$ and the pressure Hessian eigenvectors $\boldsymbol{y}_i$ is very weak. There is only a moderate tendency for alignment between $\boldsymbol{y}_{2,3}$ and $\boldsymbol{\omega}$ (Chevillard *et al.* 2008). This constitutes an obstacle for understanding the role of the anisotropic pressure Hessian in turbulence.

On the other hand, the results in figure 8 show a striking alignment between $\boldsymbol{\omega}$ and the dimensionally reduced anisotropic pressure Hessian eigenvectors $\boldsymbol{z}_i$. Indeed, there is a remarkable tendency for $\boldsymbol{z}_2$ to align with $\boldsymbol{\omega}$, that is consistent with the preferential alignment between $\boldsymbol{v}_2$ and $\boldsymbol{\omega}$ and between $\boldsymbol{z}_2$ and $\boldsymbol{v}_2$ (figure 9). In the Appendix we show results for these alignments based on the surrogate Gaussian field, and the results show that even for this case there is a strong tendency for $\boldsymbol{z}_2$ to align with $\boldsymbol{\omega}$. However, the alignment of $\boldsymbol{z}_2$ with $\boldsymbol{\omega}$ is about four times stronger in the DNS. Therefore, while part of the striking alignment behaviour is kinematic in origin, arising due to the nature of the dimensionality-reduction process used to construct $\mathcal{H}_\gamma^*$, a significant contribution also comes from the turbulence dynamics itself. It is not immediately obvious why this preferential alignment should occur even for the Gaussian field. Although the term used to perform the dimensionality reduction $\gamma[\boldsymbol{R}, \boldsymbol{S}]$ consists of a rotation of the strain-rate eigenframe about the vorticity axis, it does not trivially follow from this that $\boldsymbol{z}_2$ should exhibit preferential alignment with respect $\boldsymbol{\omega}$.

As discussed in § 2.4, the contribution of the vorticity and dimensionally reduced anisotropic pressure Hessian to the straining motion in the fluid is confined to planes. In particular, the straining associated with the centrifugal force produced by the spinning of the fluid particle about its vorticity axis acts in the plane $\Pi_{\boldsymbol{\omega}}$, orthogonal to $\boldsymbol{\omega}$, while the contribution from $\mathcal{H}_\gamma^*$ acts on the plane Π_2, orthogonal to its intermediate eigenvector $\boldsymbol{z}_2$. The results shown in figure 8(*b*) indicate that these two planes tend to almost coincide. However, the effects of $\boldsymbol{\omega}$ and $\mathcal{H}_\gamma^*$ on the strain-rate dynamics are radically different. The rotation of the fluid element generates a stretching rate of magnitude $\omega^2/4$ on the plane $\Pi_{\boldsymbol{\omega}}$ and its contribution is isotropic, since the eigenvalue of the projection tensor $\boldsymbol{P}_{\boldsymbol{\omega}}$ is the same for all the eigenvectors that belong to the plane $\Pi_{\boldsymbol{\omega}}$, as in figure 2(*b*). On the other hand, the dimensionally reduced anisotropic pressure Hessian causes a stretching rate of magnitude ψ in direction $\boldsymbol{z}_3$ and an equal and opposite compression in the direction $\boldsymbol{z}_1$, orthogonal to $\boldsymbol{z}_3$, as in figure 2(*c*). This results in a marked anisotropy of the effect of $\mathcal{H}_\gamma^*$ on the plane Π_2. Since the planes $\Pi_{\boldsymbol{\omega}}$ and Π_2 tend to be almost parallel, the anisotropic pressure Hessian can be understood to be the source of the anisotropy, which is absent in the centrifugal contribution, that plays a key role in the prevention of the blow-up that occurs in the RE system.

Interestingly, the additional term proportional to $[\boldsymbol{R}, \boldsymbol{S}]$ used in the definition of $\mathcal{H}_\gamma^*$, (2.22), arises from a rotation of the strain-rate eigenframe about $\boldsymbol{\omega}$ and the results show that $\mathcal{H}_\gamma^*$ lays on a two-dimensional manifold that statistically has a strong, but imperfect tendency to be orthogonal to $\boldsymbol{\omega}$. The dynamical significance of the slight misalignment is that it allows the anisotropic pressure Hessian to contribute to the eigenframe dynamics of the vorticity components. To see this we note that while the pressure Hessian does not explicitly contribute to the vorticity equation $D_t\boldsymbol{\omega}$, it does explicitly contribute to $D_t^2\boldsymbol{\omega}$. By neglecting the viscous term and using the dimensionally reduced anisotropic Hessian (since we are here only concerned with the single-time dynamics of the system), we may
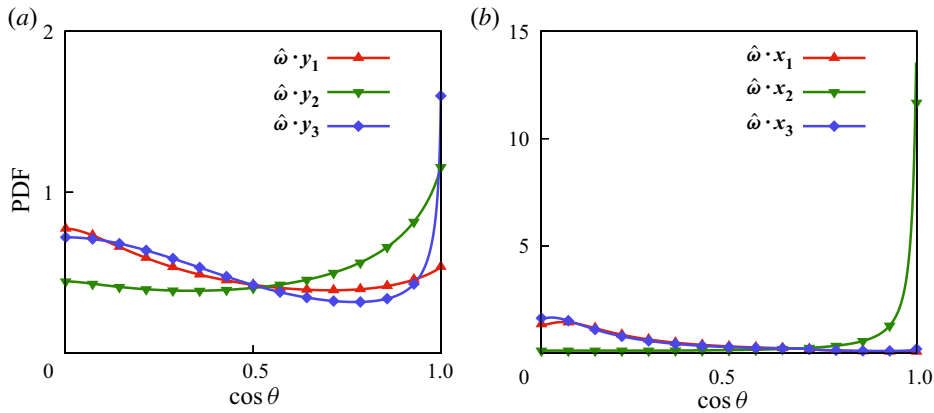
FIGURE 8. The PDF of the orientation between the vorticity vector and (*a*) the eigenframe of the pressure Hessian, (*b*) the eigenframe of the dimensionally reduced anisotropic pressure Hessian. The alignment is expressed by inner product between the normalized vorticity $\hat{\boldsymbol{\omega}} \equiv \boldsymbol{\omega}/\|\boldsymbol{\omega}\|$ and normalized eigenvectors of $\mathcal{H}$ ($\boldsymbol{y}_i$) and $\mathcal{H}^*_\gamma$ ($\boldsymbol{z}_i$).

write

$$\mathrm{D}_t^2 \boldsymbol{\omega} = -\frac{2}{3}\mathcal{Q}\boldsymbol{\omega} - \psi \left[(\boldsymbol{z}_1^\top \cdot \boldsymbol{\omega})\boldsymbol{z}_1 - (\boldsymbol{z}_3^\top \cdot \boldsymbol{\omega})\boldsymbol{z}_3 \right]. \qquad (4.1)$$

This shows that if $\boldsymbol{z}_2$ is parallel to $\boldsymbol{\omega}$, then $\mathcal{H}^*_\gamma$ does not contribute to $\mathrm{D}_t^2\boldsymbol{\omega}$. It is known that in the inviscid case, the neglect of the anisotropic pressure Hessian in the eigenframe dynamics leads to a finite time singularity (Vieillefosse 1982). Therefore, assuming that the slight misalignment between $\mathcal{H}^*_\gamma$ and $\boldsymbol{\omega}$ is not solely due to viscous effects, then this misalignment must also play a role in regularizing the eigenframe dynamics thus hindering the onset of singularities in the inviscid Euler system.

Figures 9(*a*), 9(*c*) and 9(*e*) present the statistical alignment of the eigenvectors $\boldsymbol{y}_i$ of $\mathcal{H}$, with the strain-rate eigenvectors $\boldsymbol{v}_j$. The alignments between the pressure Hessian eigenframe and the strain-rate eigenframe do not reveal any strong preferences, with weak alignment tendencies to $\boldsymbol{y}_1 \cdot \boldsymbol{v}_1 \simeq 0.71$ and $\boldsymbol{y}_{1,3} \cdot \boldsymbol{v}_3 \simeq 0.71$. Therefore, there is a very mild tendency for $\boldsymbol{y}_1$ to form a $\pi/4$ angle with $\boldsymbol{v}_1$ and $\boldsymbol{v}_3$ and for $\boldsymbol{y}_3$ to form a $\pi/4$ angle with $\boldsymbol{v}_3$. These weak alignments make it difficult to model the directionality of $\mathcal{H}$ in any simple way in terms of the eigenframe of the strain-rate tensor.

Figures 9(*b*), 9(*d*) and 9(*f*) show the alignments between the eigenvectors $\boldsymbol{z}_i$ of $\mathcal{H}^*_\gamma$, with $\boldsymbol{v}_j$. The results show, in striking contrast to the corresponding plots for the alignment of $\mathcal{H}$, that the eigenframe $\mathcal{H}^*_\gamma$ exhibits remarkable alignment properties with a strong tendency to have $\boldsymbol{z}_{1,3} \cdot \boldsymbol{v}_{1,3} \approx 0.71$, $\boldsymbol{z}_2 \cdot \boldsymbol{v}_2 \approx 1$ and $\boldsymbol{z}_2 \cdot \boldsymbol{v}_3 \approx 0$. This means that the tangent space Π_2 to the two-dimensional manifold on which $\mathcal{H}^*_\gamma$ acts tends to be orthogonal to $\boldsymbol{v}_2$. On that plane the eigenvectors $\boldsymbol{z}_1$ and $\boldsymbol{z}_3$ of $\mathcal{H}^*_\gamma$ tend to be inclined at an angle of $\pi/4$ relative to both $\boldsymbol{v}_1$ and $\boldsymbol{v}_3$. This evidence makes the dimensionally reduced anisotropic pressure Hessian suitable for modelling, since there is a well-defined most probable configuration for the orientation of $\mathcal{H}^*_\gamma$ with respect to $\boldsymbol{S}$. Those clear preferential alignments between $\boldsymbol{\omega}$ and $\boldsymbol{S}$ with $\mathcal{H}^*_\gamma$ also help to understand how the anisotropic pressure Hessian prevents blow-up, as we will discuss in the next section.

Results for the alignment between $\boldsymbol{z}_i$ and $\boldsymbol{v}_i$ based on a Gaussian surrogate field are reported in the Appendix, and show a similar striking alignment behaviour to the DNS results. However, the alignments are much weaker than the ones in the DNS. Furthermore,
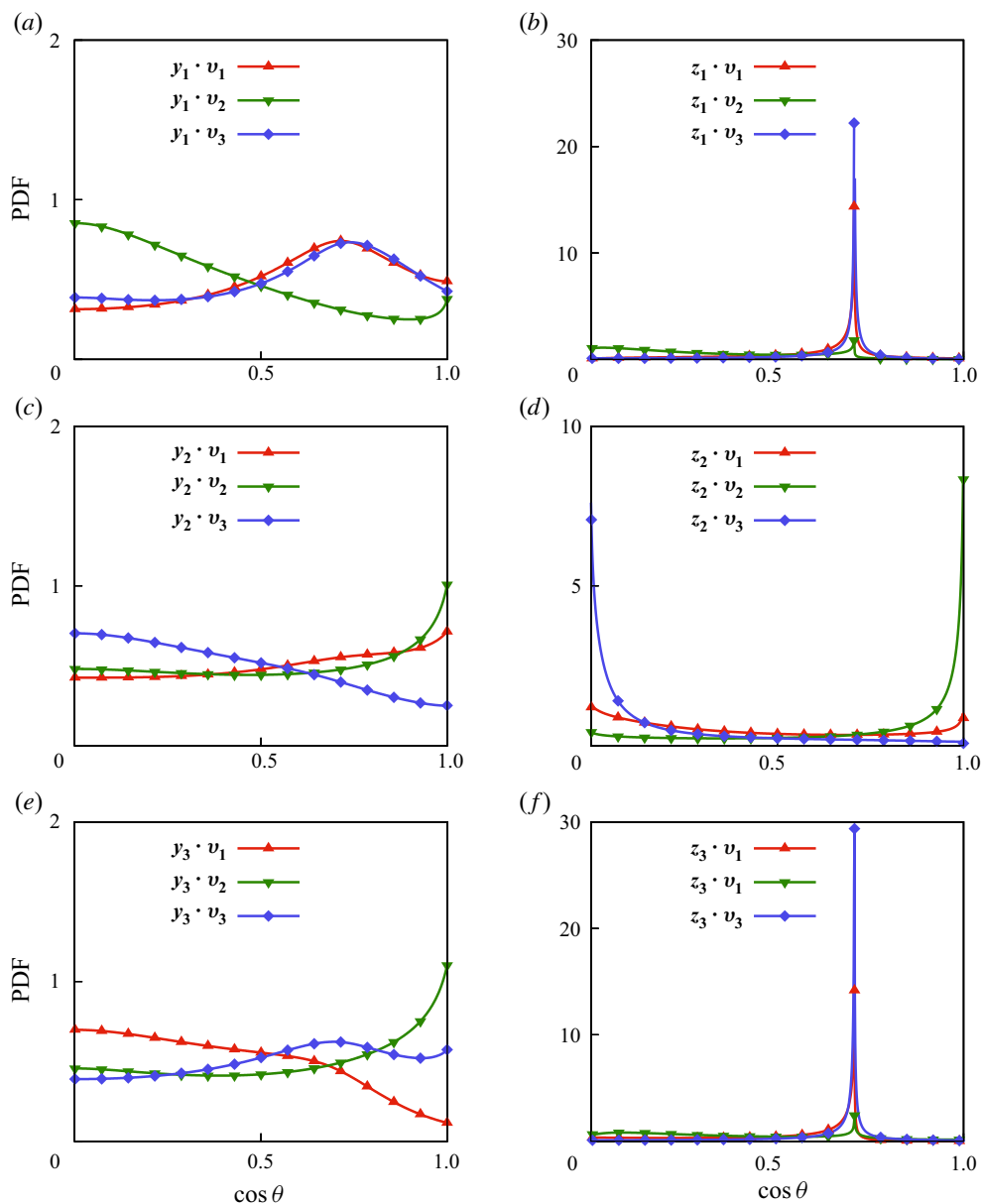
FIGURE 9. The PDF of the relative orientation between the pressure Hessian eigenframe and the strain-rate eigenframe (a, c, e) and relative orientation between the dimensionally reduced anisotropic pressure Hessian eigenframe and the strain-rate eigenframe (b, d, f). The orientation is expressed by inner product of the eigenvectors of the strain-rate tensor $\boldsymbol{v}_i$ with the eigenvectors of $\boldsymbol{\mathcal{H}}$ ($\boldsymbol{y}_i$) and the eigenvectors of $\boldsymbol{\mathcal{H}}_\gamma^*$ ($\boldsymbol{z}_i$).

while the alignments involving $\boldsymbol{v}_1$ and $\boldsymbol{v}_3$ are significantly different in the DNS, they are identical in the Gaussian field, which is most likely due to the reversibility of the latter. Therefore, just as for the alignments with vorticity, the striking alignments between $\boldsymbol{z}_i$ and $\boldsymbol{v}_i$ is partially a kinematic effect due to the form of the tensor $\gamma[\boldsymbol{R}, \boldsymbol{S}]$ used for the

dimensionality reduction, but there is also a strong and particular contribution that arises from the turbulence dynamics itself.

5. Numerical results: conditioned statistical geometry

The simpler geometry of the dimensionally reduced anisotropic pressure Hessian together with its well-defined preferential alignments can aid understanding of the role of the pressure Hessian on the dynamics of the velocity gradients. In particular, the role of the anisotropic pressure Hessian in preventing the blow-up of the RE system can be analysed by considering how the statistical alignment properties of $\mathcal{H}_\gamma^*$ depend on $\boldsymbol{S}$ and $\boldsymbol{\omega}$. The finite-time singularity prevention mechanism can be safely tackled by using $\mathcal{H}_\gamma^*$ instead of $\mathcal{H}$ since this regularity problem is associated with the behaviour of the velocity gradient invariants, and the orientation of the strain-rate eigenframe does not play any role. The equations governing λ_i, namely (2.10b), shows that there is a local stabilizing effect on the dynamical evolution of λ_i due to the centrifugal force produced by the fluid particle rotating about its vorticity axis. In particular, this term opposes the growth (in magnitude) of the compressive eigenvalue λ_3. However, it is known that this mechanism alone is not sufficient to prevent blow-up of the RE system (Meneveau 2011), and the anisotropic pressure Hessian is required to stabilize the dynamics. This can be understood more easily when the dimensionally reduced anisotropic pressure Hessian is used instead of the full anisotropic pressure Hessian. Indeed, $\mathcal{H}_\gamma^*$ is effective only on a plane which has a clear tendency to preferentially align with $\boldsymbol{S}$ and $\boldsymbol{\omega}$, in striking contrast with the mild preferential alignments of $\mathcal{H}$ with $\boldsymbol{S}$ and $\boldsymbol{\omega}$.

5.1. *Dimensionally reduced anisotropic pressure Hessian–strain-rate alignment*

The components of the dimensionally reduced anisotropic pressure Hessian, $\mathcal{H}_\gamma^*$, in the strain-rate eigenframe can be more conveniently expressed as

$$\widetilde{\mathcal{H}}_{\gamma,ij}^* = V_{ki}\mathcal{H}_{\gamma,km}^* V_{mj} = V_{ki}Z_{kp}\Psi_{pq}Z_{mq}V_{mj}, \qquad (5.1)$$

where the matrices $\boldsymbol{V}$ and $\boldsymbol{Z}$ contain the components of the strain-rate eigenvectors and dimensionally reduced pressure Hessian eigenvectors in the Cartesian basis, that is, $V_{ij} \equiv \boldsymbol{e}_i^\top \cdot \boldsymbol{v}_j$ and $Z_{ij} \equiv \boldsymbol{e}_i^\top \cdot \boldsymbol{z}_j$. The diagonal and singular matrix $\boldsymbol{\Psi}$ has on its diagonal the eigenvalues of the dimensionally reduced anisotropic pressure Hessian, $(\psi, 0, -\psi)$. The components of $\mathcal{H}_\gamma^*$ in the strain-rate eigenframe (5.1) can be written as

$$\left[\widetilde{\mathcal{H}}_{\gamma,ij}^*\right] = \psi \begin{bmatrix} \tilde{z}_{11}^2 - \tilde{z}_{13}^2 & \tilde{z}_{11}\tilde{z}_{21} - \tilde{z}_{13}\tilde{z}_{23} & \tilde{z}_{11}\tilde{z}_{31} - \tilde{z}_{13}\tilde{z}_{33} \\ \tilde{z}_{11}\tilde{z}_{21} - \tilde{z}_{13}\tilde{z}_{23} & \tilde{z}_{21}^2 - \tilde{z}_{23}^2 & \tilde{z}_{21}\tilde{z}_{31} - \tilde{z}_{23}\tilde{z}_{33} \\ \tilde{z}_{11}\tilde{z}_{31} - \tilde{z}_{13}\tilde{z}_{33} & \tilde{z}_{21}\tilde{z}_{31} - \tilde{z}_{23}\tilde{z}_{33} & \tilde{z}_{31}^2 - \tilde{z}_{33}^2 \end{bmatrix}, \qquad (5.2)$$

where $\tilde{z}_{ij} \equiv \boldsymbol{v}_i^\top \cdot \boldsymbol{z}_j$ is the ith strain-rate eigenframe component of the jth eigenvector $\boldsymbol{z}_j$ and $\sum_i \tilde{z}_{ij}^2 = 1$. Since $\mathcal{H}_\gamma^*$ acts only on the plane Π_2, spanned by $\boldsymbol{z}_1$ and $\boldsymbol{z}_3$, the expression for $\mathcal{H}_\gamma^*$ in the strain-rate eigenframe is much simpler than that for $\mathcal{H}$, in that it allows for separation of variables between the magnitude and orientation contributions. The magnitude of $\mathcal{H}_\gamma^*$ is described solely by ψ while the orientation depends on the inner products $\tilde{z}_{ij}$. The factorization into the product of a function only of the eigenvalue and a function only of the alignment of the eigenframes is a feature of two-dimensional traceless tensors, while in three dimensions such separation of variables is in general not possible (Ballouz & Ouellette 2018).

By introducing the representation (5.2) into (2.32) one obtains

$$D_t \lambda_i = -\left(\lambda_i^2 - \frac{1}{3}\sum_j \lambda_j^2\right) - \frac{1}{4}\left(\widetilde{\omega}_i^2 - \frac{1}{3}\sum_j \widetilde{\omega}_j^2\right) + \psi\left(\widetilde{z}_{i3}^2 - \widetilde{z}_{i1}^2\right). \tag{5.3}$$

It is known that the blow up of the RE model occurs in the quadrant $\mathcal{R} > 0$, $\mathcal{Q} < 0$ where the invariants $\mathcal{R}$ and $\mathcal{Q}$ are defined in (2.18). In particular, the blow-up is associated with the limit $\mathcal{R} \to +\infty$ and $\mathcal{Q} \sim -(27\mathcal{R}^2/4)^{1/3} \to -\infty$ (Vieillefosse 1982). In this quadrant the straining field is in a state of bi-axial extension, with $\lambda_1 > 0$, $\lambda_2 > 0$, $\lambda_3 < 0$. Therefore, to explore how $\mathcal{H}_\gamma^*$ prevents blow-up, we must consider its effects on the states where $\lambda_1 > 0$, $\lambda_2 > 0$, $\lambda_3 < 0$. From (5.3) we see that the contribution from $\mathcal{H}_\gamma^*$, namely $\psi(\widetilde{z}_{i3}^2 - \widetilde{z}_{i1}^2)$, will act to prevent blow-up in the quadrant $\mathcal{Q} < 0$, $\mathcal{R} > 0$ if $\widetilde{z}_{13}^2 - \widetilde{z}_{11}^2 < 0$, $\widetilde{z}_{23}^2 - \widetilde{z}_{21}^2 < 0$ and $\widetilde{z}_{33}^2 - \widetilde{z}_{31}^2 > 0$.

Figure 10 shows the average alignments between the dimensionally reduced anisotropic pressure Hessian and the strain-rate eigenframe conditioned on the principal invariants of the velocity gradient, $\langle \widetilde{z}_{i3}^2 - \widetilde{z}_{i1}^2 | \mathcal{R}, \mathcal{Q} \rangle$. The data confirm that, when $\mathcal{Q} < 0$ and $\mathcal{R} > 0$, $\langle \widetilde{z}_{23}^2 - \widetilde{z}_{21}^2 | \mathcal{R}, \mathcal{Q} \rangle < 0$ and $\langle \widetilde{z}_{33}^2 - \widetilde{z}_{31}^2 | \mathcal{R}, \mathcal{Q} \rangle > 0$, showing that $\mathcal{H}_\gamma^*$ acts to reduce $|\lambda_2|$ and $|\lambda_3|$. However, contrary to expectation, they also show that $\langle \widetilde{z}_{13}^2 - \widetilde{z}_{11}^2 | \mathcal{R}, \mathcal{Q} \rangle > 0$, such that $\mathcal{H}_\gamma^*$ explicitly acts to increase λ_1 when $\mathcal{Q} < 0$, $\mathcal{R} > 0$. Nevertheless, since $\sum_i \lambda_i = 0$, if $\mathcal{H}_\gamma^*$ acts to reduce $|\lambda_3|$ when $\mathcal{Q} < 0$, $\mathcal{R} > 0$, then it also indirectly acts to reduce λ_1, since $\lambda_1 \to \infty$ is not possible unless $|\lambda_3| \to \infty$ (noting $-\lambda_3 \geq \lambda_2$). This indirect effect is mediated via the local pressure Hessian due to the incompressibility constraint. Therefore, the effect of $\mathcal{H}_\gamma^*$ is somewhat subtle, directly acting to prevent blow-up of λ_2 and λ_3, and only indirectly acting to prevent the blow-up of λ_1. Interestingly, the direct amplification of λ_1 due to $\mathcal{H}_\gamma^*$ becomes very small in a narrow region along the right Vieillefosse tail, as the colours in figure 10(*b*) show. Therefore, this amplification mechanism is not effective in the phase space region in which the RE system blows up.

The scalar products $\widetilde{z}_{ij}$ preferentially lie in a very narrow interval around a few well-defined values, as clearly indicated by the results in figure 9. In particular, the eigenvectors z_1 and z_3 of $\mathcal{H}_\gamma^*$ tend to form an angle of $\pi/4$ with the eigenvectors v_1 and v_3 of S. Therefore, a typical configuration for the relative orientation between $\mathcal{H}_\gamma^*$ and S is

$$\left[V_{ki}Z_{kj}\right] = \begin{bmatrix} \cos(\pi/4 + \epsilon_{11}) & \sin(\epsilon_{12}) & \cos(\pi/4 + \epsilon_{13}) \\ \sin(\epsilon_{21}) & \cos(\epsilon_{22}) & \sin(\epsilon_{23}) \\ \cos(\pi/4 + \epsilon_{31}) & \sin(\epsilon_{32}) & \cos(\pi/4 + \epsilon_{33}) \end{bmatrix}, \tag{5.4}$$

where the quantities ϵ_{ij} represent the deviations of the angles from the idealized configuration considered, and there is a dependence of the sign on the angle between v_1 and z_1, which can be $\pi/4$ or $3\pi/4$ (depending upon the chosen sign of the eigenvectors). That sign does not change the discussion below. Considering only small deviations from the most probable alignment, that is, considering $|\epsilon_{ij}| \ll 1$, the elements of the rotation matrix in (5.4) can be Taylor expanded and, at first order in ϵ_{ij}, the expression for the dimensionally reduced anisotropic pressure Hessian in the strain-rate eigenframe (5.2) reduces to

$$\left[\widetilde{\mathcal{H}}_{\gamma,ij}^*\right] \sim \psi \begin{bmatrix} -2\epsilon_{11} & \epsilon_{32} & \pm 1 \\ \epsilon_{32} & 0 & \epsilon_{12} \\ \pm 1 & \epsilon_{12} & 2\epsilon_{11} \end{bmatrix}, \tag{5.5}$$
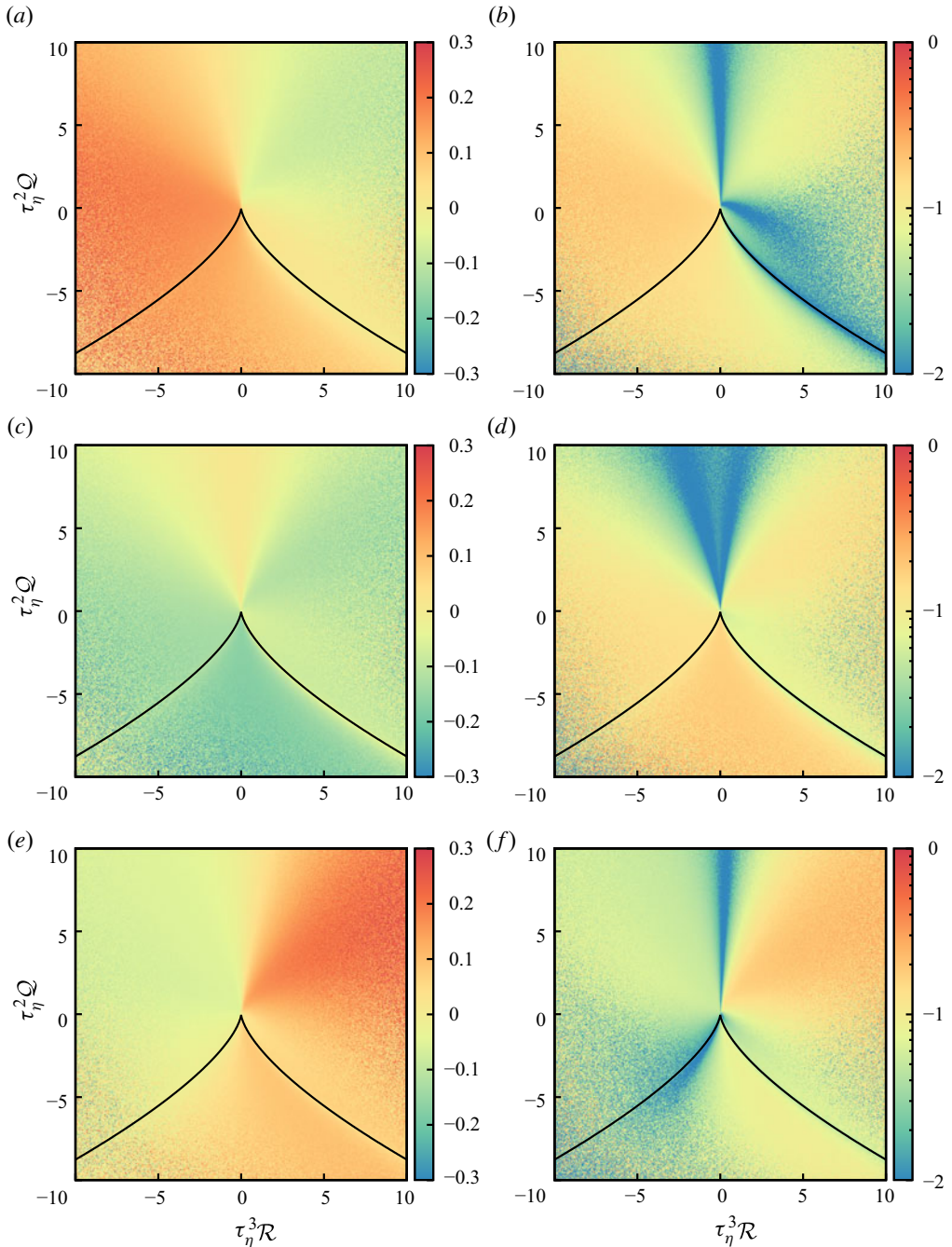
FIGURE 10. Results for $\langle \tilde{z}_{i3}^2 - \tilde{z}_{i1}^2 | \mathcal{R}, \mathcal{Q} \rangle$, (a) $i = 1$, (c) $i = 2$, (e) $i = 3$. The colour range has been truncated to $[-0.3, \ 0.3]$ in order to highlight the trend of the variables around the most probable values. Results for $\langle | \tilde{z}_{i3}^2 - \tilde{z}_{i1}^2 | | \mathcal{R}, \mathcal{Q} \rangle$ in logarithmic scale, (b) $i = 1$, (d) $i = 2$, (f) $i = 3$. Black lines denote the Vieillefosse tails.
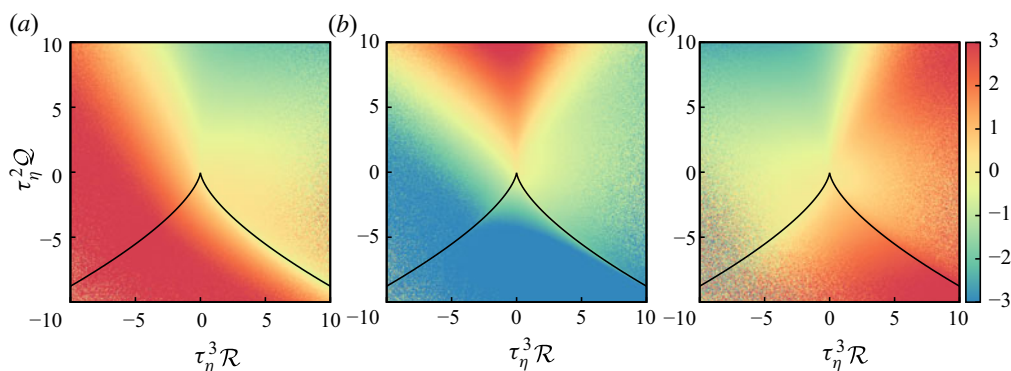
FIGURE 11. Results for $\langle -\widetilde{\mathcal{H}}^*_{\gamma, i(i)} | \mathcal{R}, \mathcal{Q} \rangle$, the average of the diagonal components of $-\mathcal{H}^*_\gamma$ in the strain-rate eigenframe conditioned on the principal invariants $\mathcal{R}, \mathcal{Q}$. (*a*) $i = 1$, (*b*) $i = 2$, (*c*) $i = 3$. Black lines denote the Vieillefosse tails.

where the orthonormality constraint, $\boldsymbol{V} \cdot \boldsymbol{V}^\top = \boldsymbol{I}$, has been used to relate the small perturbation angles. It is the diagonal components of $\mathcal{H}^*_\gamma$ that contribute directly to the rate of change of the strain-rate eigenvalues, as in (5.3), and the anisotropic pressure Hessian has no direct effect on the strain-rate eigenvalues when the most probable alignments, $\epsilon_{ij} = 0$, occur. At the level of this first-order approximation, the effect of $\mathcal{H}^*_\gamma$ on the first and third eigenvalue always has the opposite sign, which is consistent with the stabilizing effect of the pressure Hessian. Therefore, according to this first-order approximation, the pressure Hessian tends to counteract both λ_1 and λ_3 by imposing a negative rate of change of λ_1 and a positive rate of change of λ_3, such that both the most positive and negative eigenvalues are pulled toward smaller magnitudes. The results in figure 10 confirm this prediction in the $\mathcal{Q} > 0, \mathcal{R} > 0$ quadrant, where it is seen that $\mathcal{H}^*_\gamma$ acts to suppress the magnitudes of both λ_1 and λ_3. That the linearized prediction fails in the region $\mathcal{Q} < 0, \mathcal{R} > 0$ is perhaps not surprising since that is the region of most intense nonlinear activity, and where $\mathcal{H}^*_\gamma$ must be sufficiently large (and by implication ϵ_{ij} cannot be too small) in order to counteract the blow-up associated with the RE dynamics. The linearization also predicts that the influence of $\mathcal{H}^*_\gamma$ on λ_2 is only a second-order effect when ϵ_{ij} is small. However, this prediction is in general not supported by the DNS, since the results in figure 10 show that in most of the $\mathcal{Q}, \mathcal{R}$ plane, $\mathcal{H}^*_\gamma$ strongly hinders the growth of positive λ_2.

In order to fully quantify the effect of $\mathcal{H}^*_\gamma$, its magnitude should also be considered together with its orientation. The average of the diagonal components of $-\mathcal{H}^*_\gamma$ in the strain-rate eigenframe conditioned on the invariants $\mathcal{R}, \mathcal{Q}$ is shown in figure 11. Despite the large magnitude of the eigenvalue of $\mathcal{H}^*_\gamma$, the contribution of $\mathcal{H}^*_\gamma$ to the strain-rate eigenvalue dynamics is moderate on average. Figure 7 shows that the eigenvalue of $\mathcal{H}^*_\gamma$, namely ψ, is very large along the right Vieillefosse tail and in the quadrant $\mathcal{Q} > 0, \mathcal{R} < 0$. Figures 10(*a*)–10(*c*) show that $\langle |\tilde{z}^2_{i3} - \tilde{z}^2_{i1}| | \mathcal{R}, \mathcal{Q} \rangle$ is small along the right Vieillefosse tail, and these small values of $|\tilde{z}_{i3} - \tilde{z}_{i1}|$ compensate the large magnitude of ψ in the same region. In particular, the orientational contribution of $\mathcal{H}^*_\gamma$ to the dynamics of λ_1, namely $|\tilde{z}_{13} - \tilde{z}_{11}|$, is very small along the right Vieillefosse tail. This indicates how the direct amplification of λ_1 due to $\mathcal{H}^*_\gamma$ does not lead to blow up, since this amplification is strong for $\mathcal{R} < 0$, but is very weak along the right Vieillefosse tail where RE blows up, as shown in figure 11(*a*). As observed above, the dimensionally reduced anisotropic pressure Hessian tends to suppress positive values of λ_2 in the $\mathcal{R} > 0, \mathcal{Q} < 0$ quadrant, as displayed
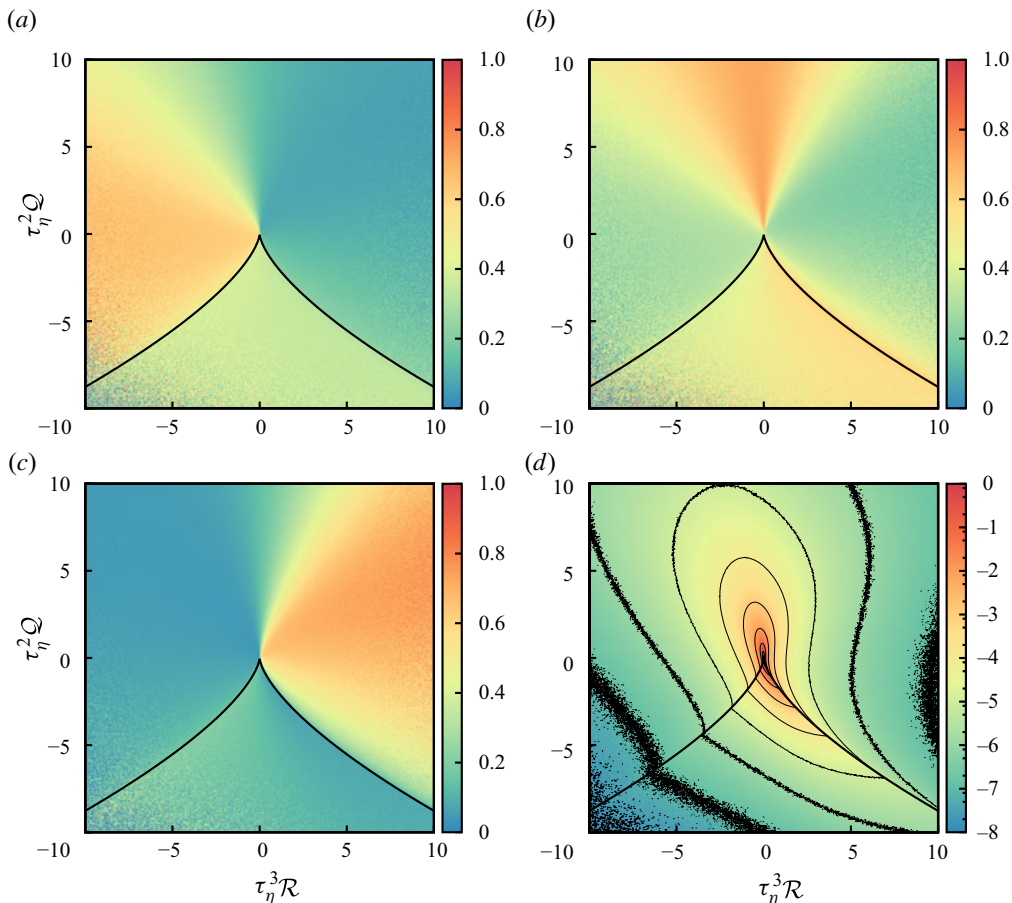
(a)

(b)

(c)

(d)

FIGURE 12. Results for $\langle (\hat{\boldsymbol{\omega}} \cdot \boldsymbol{v}_i)^2 | \mathcal{R}, \mathcal{Q} \rangle$, the statistical alignment between vorticity and eigenvectors of the strain-rate tensor, conditioned on the principal invariants $\mathcal{R}, \mathcal{Q}$. (a) $i = 1$, (b) $i = 2$, (c) $i = 3$. Panel (d) shows the joint probability density of the principal invariants $\mathcal{R}$ and $\mathcal{Q}$. Black lines denote the Vieillefosse tails.

in figure 11(b). Interestingly, however, $\mathcal{H}_\gamma^*$ contributes to the growth of positive λ_2 in the region $\mathcal{Q} > 0$, $\mathcal{R} < 0$, where $\boldsymbol{\omega}$ and $\boldsymbol{v}_2$ are also strongly aligned (see figure 12b). As such, $\mathcal{H}_\gamma^*$ indirectly contributes to vortex stretching. The results in figure 11(c) show that, the dimensionally reduced anisotropic pressure Hessian strongly hinders λ_3 along the right Vieillefosse tail, contributing to its amplification only in a small region where $\mathcal{R} < 0$ and $\mathcal{Q} > 0$. This is a key way in which $\mathcal{H}_\gamma^*$ acts to prevent blow-up in the region $\mathcal{R} > 0$, $\mathcal{Q} < 0$.

5.2. *Dimensionally reduced anisotropic pressure Hessian–vorticity alignment*

As shown earlier, $\mathcal{H}_\gamma^*$ exhibits remarkable alignment properties with respect to the vorticity $\boldsymbol{\omega}$. In view of this, we now consider how this alignment impacts the way that $\mathcal{H}_\gamma^*$ competes with the centrifugal term produced by vorticity to control the growth of the strain rates. This can be explored by considering the strain rates along the vorticity direction.
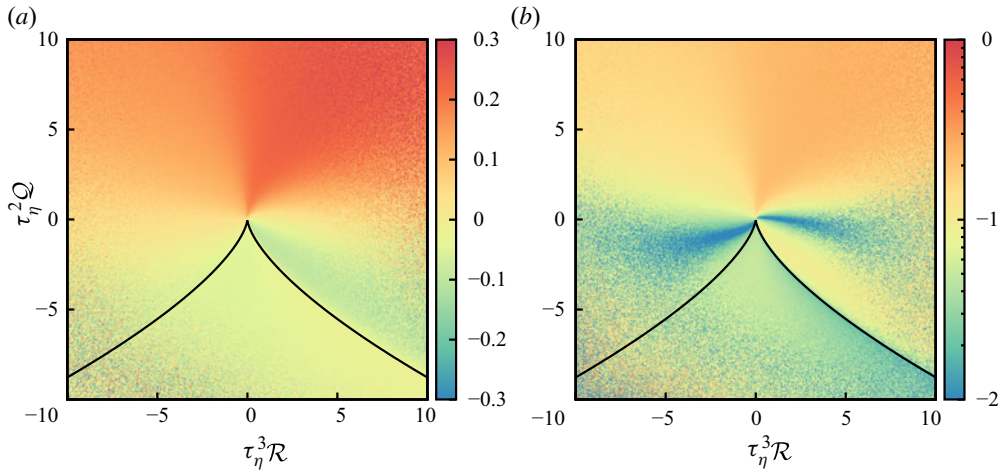
FIGURE 13. Statistical alignment between vorticity and eigenvectors of the dimensionally reduced anisotropic pressure Hessian, conditioned on the principal invariants $\mathcal{R}, \mathcal{Q}$. Results for (a) $\langle (\hat{\boldsymbol{\omega}} \cdot \boldsymbol{z}_3)^2 - (\hat{\boldsymbol{\omega}} \cdot \boldsymbol{z}_1)^2 | \mathcal{R}, \mathcal{Q} \rangle$ and (b) $\langle |(\hat{\boldsymbol{\omega}} \cdot \boldsymbol{z}_3)^2 - (\hat{\boldsymbol{\omega}} \cdot \boldsymbol{z}_1)^2| | \mathcal{R}, \mathcal{Q} \rangle$ in logarithmic scale. Black lines denote the Vieillefosse tails.

The statistical alignments of the vorticity vector with the strain-rate eigenvectors, quantified by $(\boldsymbol{v}_i \cdot \hat{\boldsymbol{\omega}})^2$, conditioned on the invariants $\mathcal{R}$ and $\mathcal{Q}$, are shown in figure 12. The vorticity tends to align with the most extensional strain-rate eigenvector in the region $\mathcal{R} < 0$ and also, to a lesser extent, between the Vieillefosse tails. Alignment between the vorticity and the most compressional strain-rate eigenvector takes place in the region $\mathcal{R} > 0$ only, above the right Vieillefosse tail. The vorticity vector strongly aligns with the intermediate strain-rate eigenvector in the region $\mathcal{Q} > 0$, close to the $\mathcal{R} = 0$ axis and along the right Vieillefosse tail. The half-plane $\mathcal{Q} > 0$ and the vicinity of the right Vieillefosse tail correspond to the bulk of probability on the $\mathcal{Q}, \mathcal{R}$ plane (Meneveau 2011), as shown in figure 12(d), and therefore preferential alignment between vorticity and the intermediate strain-rate eigenvector is observed. In the $\mathcal{Q} > 0$ region where the alignment between vorticity and the intermediate strain-rate eigenvector is strong, the contribution of $\mathcal{H}_\gamma^*$ to the dynamics of λ_2 is also strong and positive (see figure 11b). Therefore, $\mathcal{H}_\gamma^*$ plays an important indirect role in the stretching of vorticity by the intermediate eigenvalue in this region.

We now turn to the combined effects of $\mathcal{H}_\gamma^*$ and $\boldsymbol{\omega}$ on the strain-rate dynamics. The evolution equation for $\boldsymbol{S}$ may be written as (ignoring the viscous term)

$$\mathrm{D}_t \boldsymbol{S} = -\left(\boldsymbol{S} \cdot \boldsymbol{S} - \frac{1}{3} \mathrm{Tr}(\boldsymbol{S} \cdot \boldsymbol{S}) \boldsymbol{I} \right) - \frac{1}{4} \left(\boldsymbol{\omega}\boldsymbol{\omega}^\top - \frac{1}{3}\omega^2 \boldsymbol{I} \right) - \mathcal{H}. \qquad (5.6)$$

When we consider the projection of this equation along the instantaneous vorticity direction $\hat{\boldsymbol{\omega}} \equiv \boldsymbol{\omega}/\omega$, the contribution of the last two terms on the right-hand side of (5.6) is

$$\hat{\boldsymbol{\omega}}^\top \cdot \left(-\frac{1}{4} \boldsymbol{\omega}\boldsymbol{\omega}^\top + \frac{1}{12}\omega^2 \boldsymbol{I} - \mathcal{H} \right) \cdot \hat{\boldsymbol{\omega}} = -\frac{1}{6}\omega^2 + \psi \left((\hat{\boldsymbol{\omega}} \cdot \boldsymbol{z}_3)^2 - (\hat{\boldsymbol{\omega}} \cdot \boldsymbol{z}_1)^2 \right), \qquad (5.7)$$

where the properties of $\mathcal{H}_\gamma^*$ have allowed us to replace $\mathcal{H}$ with $\mathcal{H}_\gamma^*$ on the right-hand side of (5.7). Note that the term $-\omega^2/6$ comes entirely from the contribution of vorticity to the

isotropic part of the pressure Hessian, since the centrifugal contribution does not act along the direction of vorticity, but only in directions orthogonal to it. Equation (5.7) shows that (notice that $\psi \geq 0$) when the vorticity is more aligned with the extensional/compressional direction of $\mathcal{H}_\gamma^*$, then $\mathcal{H}_\gamma^*$ acts with/against the contribution from vorticity to oppose/aid the production of strain rate along the vorticity direction. In figure 13 we consider the DNS data for $\langle (\hat{\boldsymbol{\omega}} \cdot \boldsymbol{z}_3)^2 - (\hat{\boldsymbol{\omega}} \cdot \boldsymbol{z}_1)^2 | \mathcal{R}, \mathcal{Q} \rangle$. The results show that, in $\mathcal{Q} > 0$ regions, the vorticity vector preferentially aligns with the most compressional eigenvector of $\mathcal{H}_\gamma^*$, so that $\langle (\hat{\boldsymbol{\omega}} \cdot \boldsymbol{z}_3)^2 - (\hat{\boldsymbol{\omega}} \cdot \boldsymbol{z}_1)^2 | \mathcal{R}, \mathcal{Q} \rangle > 0$. On the contrary, in $\mathcal{Q} < 0$ regions $\langle (\hat{\boldsymbol{\omega}} \cdot \boldsymbol{z}_3)^2 - (\hat{\boldsymbol{\omega}} \cdot \boldsymbol{z}_1)^2 | \mathcal{R}, \mathcal{Q} \rangle < 0$. This striking behaviour means that in vorticity dominated regions, the dynamical effect of $\mathcal{H}_\gamma^*$ is to increase the strain rate along the vorticity direction, and the opposite in strain-rate-dominated regions.

6. Conclusions

In this paper a new symmetry for the dynamics of the velocity gradient invariants has been presented, and it has been interpreted as a symmetry transformation for the anisotropic pressure Hessian. This symmetry transformation arises because the dynamics of the strain-rate eigenvalues and vorticity components in the strain-rate eigenframe are unaffected by the angular velocity of the eigenframe along the vorticity direction. Using this symmetry, we have introduced a transformed pressure Hessian, $\mathcal{H}_\gamma$, that is the sum of the standard pressure Hessian and the additional term $[\boldsymbol{R}, \boldsymbol{S}]$, which is the commutator between the rotation-rate and strain-rate tensors. We then sought for lower-dimensional representations of the pressure Hessian by performing a dimensionality reduction on $\mathcal{H}_\gamma$, allowed by the additional degree of freedom provided by the symmetry transformation. Remarkably, this dimensional reduction is possible everywhere in the flow except on sets of zero measure, and consequently almost everywhere in the flow a two-dimensional form of $\mathcal{H}_\gamma$ may be defined, which we denote by $\mathcal{H}_\gamma^*$, that generates exactly the same eigenframe dynamics as the full three-dimensional pressure Hessian $\mathcal{H}$. We also showed that $\mathcal{H}_\gamma^*$ exhibits remarkable alignment properties with respect to the strain-rate eigenframe and vorticity, that are not possessed by $\mathcal{H}$. In particular, the plane on which $\mathcal{H}_\gamma^*$ acts tends to be almost orthogonal to the vorticity vector. Consistently, the intermediate eigenvector of $\mathcal{H}_\gamma^*$ strongly aligns with the strain-rate intermediate eigenvector. Also, the most compressional/extensional eigenvectors of $\mathcal{H}_\gamma^*$ preferentially form an angle of $\pi/4$ with the most compressional/extensional eigenvectors of the strain-rate tensor. We showed that these alignments may be partially observed even in a Gaussian surrogate field formed by randomizing the Fourier phases in the DNS velocity field. This indicates that part of the cause of the alignments is the mathematical structure of the symmetry transformation used in constructing $\mathcal{H}_\gamma^*$. However, the alignments are much stronger in the DNS than for the Gaussian field, and there are several important qualitative differences. This shows that the genuine dynamical properties of turbulence are playing a strong role in the striking alignments observed.

The dimensionally reduced anisotropic pressure Hessian offers promising applications. For example, the reduction in dimensionality, provided by replacing $\mathcal{H}$ with $\mathcal{H}_\gamma^*$ in the eigenframe equations, is a step towards more efficient modelling, since the dimensionally reduced anisotropic pressure Hessian can be specified by only four scalar quantities instead of five required by the fully three-dimensional $\mathcal{H}$. The eigenvalues of $\mathcal{H}_\gamma^*$ are also shown to be strongly related to the local strain rate and vorticity in the flow, suggesting relatively simple ways to model these eigenvalues in Lagrangian models for the velocity gradient tensor. This property, together with the reduction in dimensionality and the remarkable
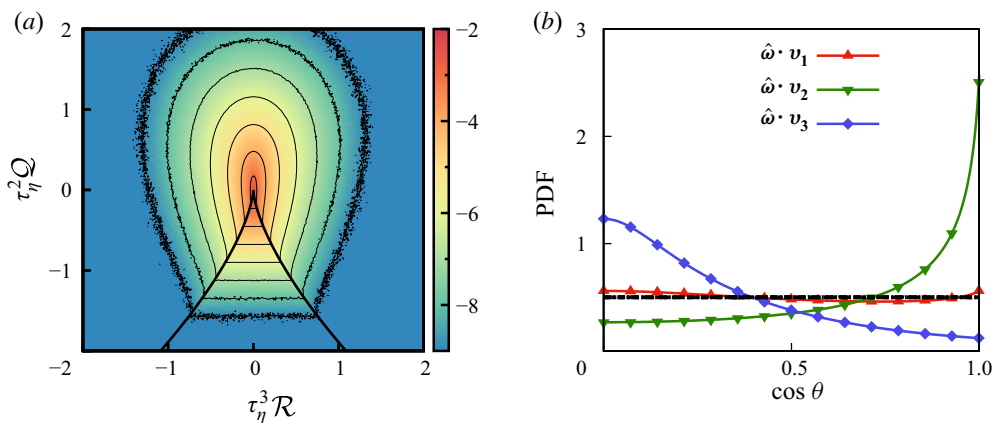
FIGURE 14. (*a*) Joint probability density function of the second and third principal invariants of the velocity gradient in the Gaussian surrogate field. (*b*) Alignment between strain-rate eigenvectors $\boldsymbol{v}_i$ and normalized vorticity $\hat{\boldsymbol{\omega}} \equiv \boldsymbol{\omega}/\|\boldsymbol{\omega}\|$ in the DNS (red, green and blue curves) and surrogate (black curves) fields.

alignment properties of $\mathcal{H}_\gamma^*$, offer promising insights into ways in which the anisotropic pressure Hessian and its effects on the eigenframe dynamics can be modelled. The development of such a model will be the subject of a future work.

Acknowledgements

Declaration of interests

The authors report no conflict of interest.

Appendix. Dimensionally reduced pressure Hessian in a Gaussian field

In §4 we presented the statistical alignment of the dimensionally reduced pressure Hessian $\mathcal{H}_\gamma^*$ with the vorticity and the strain-rate eigenvectors in a DNS of homogeneous and isotropic turbulence. In this appendix, we compute the same results using a Gaussian surrogate field in order to compare with the DNS results. The aim is to understand the extent to which the remarkable alignments observed are due to the turbulence dynamics, and how much might have a kinematic origin (i.e. may be observed even for a Gaussian field).

A surrogate Gaussian field is built from a DNS field by randomizing the Fourier phases of the velocity field, while retaining the Fourier amplitudes from the DNS. In figure 14 we show the PDF of $\mathcal{Q}, \mathcal{R}$, highlighting the symmetry about $\mathcal{R} = 0$ for this surrogate field, and also the PDFs of the alignments between vorticity and the strain-rate eigenvectors, confirming that there is no preferential alignment in this Gaussian field.

In figure 15 the PDFs of $\det[\boldsymbol{R}, \boldsymbol{S}]$ and γ are shown. The distribution of $\det[\boldsymbol{R}, \boldsymbol{S}]$ remains narrow for the surrogate field, as expected. The PDF of γ is quite strongly non-Gaussian even for the surrogate field, but the non-Gaussianity is much smaller than for
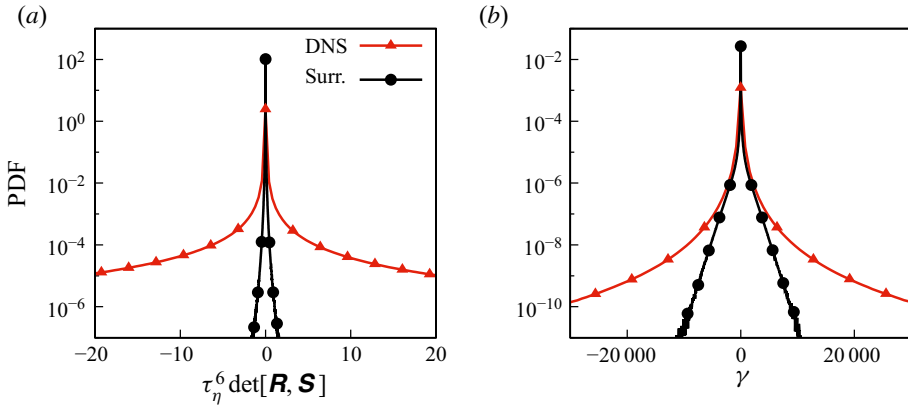
FIGURE 15. (*a*) Probability density function of det[**R**, **S**], in the surrogate field and DNS. (*b*) The PDF of the real and finite multipliers γ in the surrogate field and DNS.
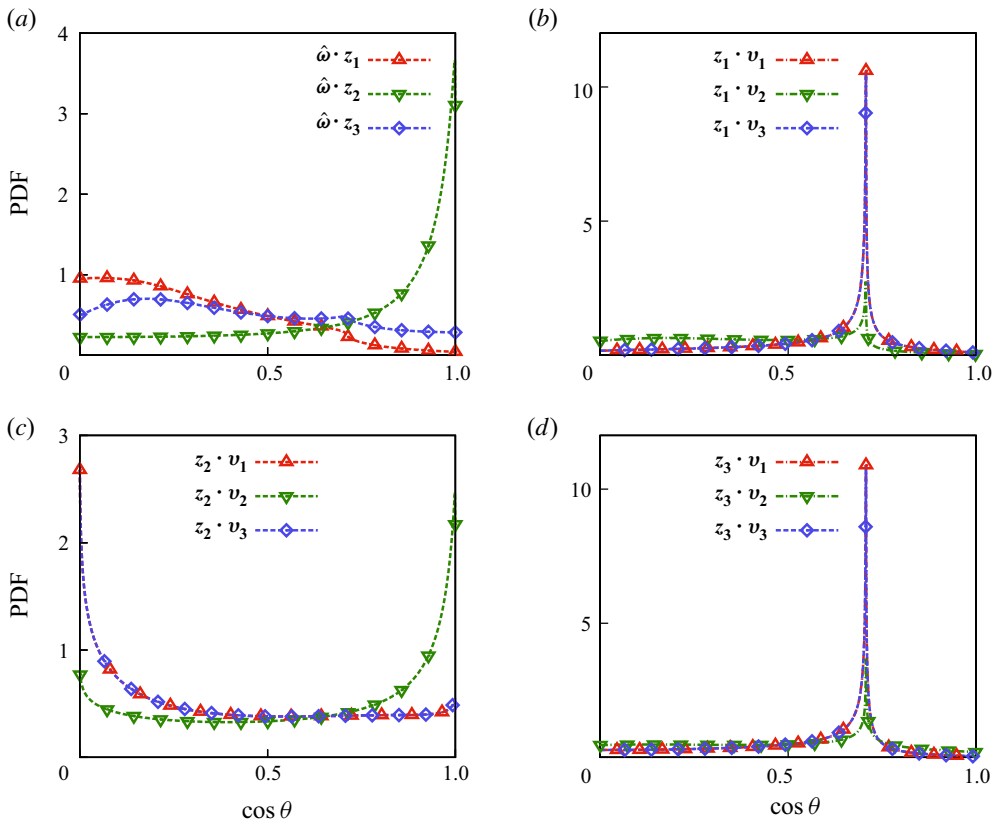

FIGURE 16. (*a*) The PDF of the orientation between the vorticity vector and the eigenframe of the dimensionally reduced pressure Hessian for the surrogate field. (*b*)–(*d*) Orientation between the eigenframe of the dimensionally reduced pressure Hessian and the strain-rate eigenframe for the surrogate field.

the DNS observed in figure 15, with very large γ being much more probable in the DNS turbulent field than in the surrogate field. Therefore, large values of γ are in part produced by the nonlinear dependence of the polynomial defining γ on the velocity gradients, but also by the intermittency of the turbulent field.

In figure 16 we show the alignments between the eigenvectors of the dimensionally reduced pressure Hessian z_i and the normalized vorticity $\hat{\omega} \equiv \omega/\|\omega\|$, and between z_i and the strain-rate eigenvectors v_i for the surrogate field. Comparing with the corresponding DNS results in figures 8 and 9, we find that while some of the striking alignment observed in the DNS can also be seen for surrogate field, the alignments in the surrogate field are considerably weaker than in the DNS. In addition to these strong quantitative differences, there are also some important qualitative differences. For example, in the DNS results, z_2 shows almost no preferential alignment with v_1, but strong misalignment with v_3. In the surrogate field, however, the alignments between z_2 and v_1, and z_2 and v_3 appear identical. This is most likely due to the reversibility of the surrogate field, in contrast to the irreversible turbulent flow in the DNS. Therefore, part of the reason why $\mathcal{H}_\gamma^*$ lives on a two-dimensional manifold that is almost orthogonal to both $\hat{\omega}$ and v_2 is simply due to the mathematical structure of the symmetry transformation used in constructing $\mathcal{H}_\gamma^*$. However, a strong contribution to the striking alignment observed in the DNS does genuinely arise from the actual turbulence dynamics.

REFERENCES

ANDERSON, E., BAI, Z., BISCHOF, C., BLACKFORD, S., DEMMEL, J., DONGARRA, J., DU CROZ, J., GREENBAUM, A., HAMMARLING, S., MCKENNEY, A., *et al.* 1999 *LAPACK Users' Guide*, 3rd edn. Society for Industrial and Applied Mathematics.

ASHURST, W. T., KERSTEIN, A. R., KERR, R. M. & GIBSON, C. H. 1987 Alignment of vorticity and scalar gradient with strain rate in simulated Navier–Stokes turbulence. *Phys. Fluids* **30** (8), 2343–2353.

BALLOUZ, J. G. & OUELLETTE, N. T. 2018 Tensor geometry in the turbulent cascade. *J. Fluid Mech.* **835**, 1048–1064.

BETCHOV, R. 1956 An inequality concerning the production of vorticity in isotropic turbulence. *J. Fluid Mech.* **1** (5), 497–504.

BIFERALE, L., MENEVEAU, C. & VERZICCO, R. 2014 Deformation statistics of sub-Kolmogorov-scale ellipsoidal neutrally buoyant drops in isotropic turbulence. *J. Fluid Mech.* **754**, 184–207.

BUARIA, D., PUMIR, A., BODENSCHATZ, E. & YEUNG, P. K. 2019 Extreme velocity gradients in turbulent flows. *New J. Phys.* **21** (4), 043004.

CANTWELL, B. J. 1992 Exact solution of a restricted Euler equation for the velocity gradient tensor. *Phys. Fluids* A **4** (4), 782–793.

CHERTKOV, M., PUMIR, A. & SHRAIMAN, B. I. 1999 Lagrangian tetrad dynamics and the phenomenology of turbulence. *Phys. Fluids* **11** (8), 2394–2410.

CHEVILLARD, L. & MENEVEAU, C. 2006 Lagrangian dynamics and statistical geometric structure of turbulence. *Phys. Rev. Lett.* **97**, 174501.

CHEVILLARD, L. & MENEVEAU, C. 2013 Orientation dynamics of small, triaxial-ellipsoidal particles in isotropic turbulence. *J. Fluid Mech.* **737**, 571–596.

CHEVILLARD, L., MENEVEAU, C., BIFERALE, L. & TOSCHI, F. 2008 Modeling the pressure Hessian and viscous Laplacian in turbulence: comparisons with direct numerical simulation and implications on velocity gradient dynamics. *Phys. Fluids* **20** (10), 101504.

DRESSELHAUS, E. & TABOR, M. 1992 The kinematics of stretching and alignment of material elements in general flow fields. *J. Fluid Mech.* **236**, 415–444.

FALKOVICH, G. & GAWĘDZKI, K. 2014 Turbulence on hyperbolic plane: the fate of inverse cascade. *J. Stat. Phys.* **156** (1), 10–54.

GIRIMAJI, S. S. & POPE, S. B. 1990 A diffusion model for velocity gradients in turbulence. *Phys. Fluids* A **2** (2), 242–256.

IBBEKEN, G., GREEN, G. & WILCZEK, M. 2019 Large-scale pattern formation in the presence of small-scale random advection. *Phys. Rev. Lett.* **123**, 114501.

IRELAND, P. J., BRAGG, A. D. & COLLINS, L. R. 2016*a* The effect of Reynolds number on inertial particle dynamics in isotropic turbulence. Part 1. Simulations without gravitational effects. *J. Fluid Mech.* **796**, 617–658.

IRELAND, P. J., BRAGG, A. D. & COLLINS, L. R. 2016*b* The effect of Reynolds number on inertial particle dynamics in isotropic turbulence. Part 2. Simulations with gravitational effects. *J. Fluid Mech.* **796**, 659–711.

IRELAND, P. J., VAITHIANATHAN, T., SUKHESWALLA, P. S., RAY, B. & COLLINS, L. R. 2013 Highly parallel particle-laden flow solver for turbulence research. *Comput. Fluids* **76**, 170–177.

JOHNSON, P. L. & MENEVEAU, C. 2015 Large-deviation joint statistics of the finite-time Lyapunov spectrum in isotropic turbulence. *Phys. Fluids* **27** (8), 085110.

JOHNSON, P. L. & MENEVEAU, C. 2016 A closure for lagrangian velocity gradient evolution in turbulence using recent-deformation mapping of initially Gaussian fields. *J. Fluid Mech.* **804**, 387–419.

JOHNSON, P. L. & MENEVEAU, C. 2017 Turbulence intermittency in a multiple-time-scale Navier–Stokes-based reduced model. *Phys. Rev. Fluids* **2**, 072601.

LAWSON, J. M. & DAWSON, J. R. 2015 On velocity gradient dynamics and turbulent structure. *J. Fluid Mech.* **780**, 60–98.

MAJDA, A. J. & BERTOZZI, A. L. 2001 *Vorticity and Incompressible Flow*. Cambridge University Press.

MENEVEAU, C. 2011 Lagrangian dynamics and models of the velocity gradient tensor in turbulent flows. *Annu. Rev. Fluid Mech.* **43** (1), 219–245.

NASO, A. & PUMIR, A. 2005 Scale dependence of the coarse-grained velocity derivative tensor structure in turbulence. *Phys. Rev.* E **72**, 056318.

NOMURA, K. K. & POST, G. K. 1998 The structure and dynamics of vorticity and rate of strain in incompressible homogeneous turbulence. *J. Fluid Mech.* **377**, 65–97.

OHKITANI, K. 1993 Eigenvalue problems in three-dimensional Euler flows. *Phys. Fluids* A **5** (10), 2570–2572.

POPE, S. B. 2000 *Turbulent Flows*. Cambridge University Press.

TOWNS, J., COCKERILL, T., DAHAN, M., FOSTER, I., GAITHER, K., GRIMSHAW, A., HAZLEWOOD, V., LATHROP, S., LIFKA, D., PETERSON, G. D., *et al.* 2014 XSEDE: accelerating scientific discovery. *Comput. Sci. Engng* **16** (5), 62–74.

TSINOBER, A. 2001 *An Informal Introduction to Turbulence*. Kluwer Academic.

VIEILLEFOSSE, P. 1982 Local interaction between vorticity and shear in a perfect incompressible fluid. *J. Phys. France* **43** (6), 837–842.

VIEILLEFOSSE, P. 1984 Internal motion of a small element of fluid in an inviscid flow. *Physica* A **125** (1), 150–162.

VLAYKOV, D. G. & WILCZEK, M. 2019 On the small-scale structure of turbulence and its impact on the pressure field. *J. Fluid Mech.* **861**, 422–446.

WILCZEK, M. & MENEVEAU, C. 2014 Pressure hessian and viscous contributions to velocity gradient statistics based on Gaussian random fields. *J. Fluid Mech.* **756**, 191–225.

YEUNG, P. K., DONZIS, D. A. & SREENIVASAN, K. R. 2012 Dissipation, enstrophy and pressure statistics in turbulence simulations at high Reynolds numbers. *J. Fluid Mech.* **700**, 5–15.

YU, H. & MENEVEAU, C. 2010 Lagrangian refined kolmogorov similarity hypothesis for gradient time evolution and correlation in turbulent flows. *Phys. Rev. Lett.* **104**, 084502.